

Università degli studi di Padova
Dipartimento di Fisica e Astronomia

Tesi di Dottorato

Search for heavy resonances decaying into a Z boson and a vector boson in the $\nu\bar{\nu}$ $q\bar{q}$ final state at CMS

Supervisor: Prof. Franco Simonetto
Candidate: Lisa Benato

Scuola di Dottorato di Ricerca, XXX ciclo

"I have no special talent. I am only passionately curious."
(A. Einstein)

Contents

1	Introduction	1
2	Theoretical motivation	3
2.1	Beyond Standard Model theories	3
2.2	Heavy Vector Triplet	5
2.2.1	Simplified Lagrangian	5
2.2.2	Mass eigenstates, mixing parameters and decay widths	6
2.2.3	HVT production	10
2.2.4	Benchmark model A: weak coupling scenario	11
2.2.5	Benchmark model B: strong coupling scenario	12
2.2.6	Search for HVT resonances at LHC	13
2.3	Warped extra dimension	16
2.3.1	Randall-Sundrum original model (RS1)	16
2.3.2	Bulk extension of RS1: graviton production and decays	19
2.3.3	Search for KK bulk gravitons at LHC	22
3	The Large Hadron Collider and the CMS experiment	25
3.1	The Large Hadron Collider	25
3.1.1	Interazioni protone-protone	27
3.2	CMS detector	29
3.2.1	Il sistema di coordinate	29
3.2.2	Il solenoide	30
3.2.3	I tracciatori	32
3.2.4	Il calorimetro elettromagnetico	33
3.2.5	Il calorimetro adronico	34
3.2.6	Sistema per l'identificazione dei muoni	35
3.2.7	Altri rivelatori	37
3.2.8	Sistema di trigger	37
3.2.9	Il sistema di calcolo	38
3.3	ATLAS, ALICE, LHCb	39
3.3.1	ATLAS vs CMS	39

3.3.2	Altri esperimenti	40
4	Data and Monte Carlo samples	41
5	Physics objects	43
5.1	Vertex and Pile-up	43
5.2	Electrons	44
5.3	Muons	44
5.4	Taus	46
5.5	Photons	46
5.6	Jets	47
5.6.1	Jet mass	50
5.6.2	Jet substructure	51
5.7	b-tagging	52
5.8	Missing Energy	52
6	Diboson candidate reconstruction	55
7	Background estimation	57
8	Systematic uncertainties	59
9	Results	61
10	Conclusions	63

CONTENTS

1

Abstract

2

3

CONTENTS

Introduction

7 This analysis searches for signal of heavy resonances decaying into a pair of heavy vector
8 bosons. One Z boson is identified through its invisible decay ($\nu\nu$), while the other is required
9 to decay hadronically into a pair of quarks. The final states probed by this analysis therefore
10 consists in two quarks and two neutrinos, reconstructed as missing transverse energy (met).
11 The hadronically decaying boson (Z, W) is reconstructed as a fat jet, whose mass is used to
12 define the signal region. Two purity categories are exploited, based on the n-subjettiness of the
13 fat jet.

14 The search is performed by examining the distribution of the diboson reconstructed trans-
15 verse mass of the resonance VZ (mtVZ) for a localized excess. The shape and normalization
16 of the main background of the analysis (V+jets) are estimated with an hybrid approach using
17 the distribution of data in the sidebands, corrected for a function accounting for potential
18 differences between the signal region and the sidebands, while the minor background sources
19 are taken from simulations.

Theoretical motivation

23 The standard model (SM) of particles represents, so far, the best available description of the
 24 particles and their interactions. It is the summation of two gauge theories: the electroweak
 25 interaction, that portrays the weak and electromagnetic interactions together, and the strong
 26 interaction, or Quantum Chromodynamics (QCD). Particles, namely quarks and leptons, are
 27 described as spin 1/2 fermions, whilst interactions are represented by spin 1 bosons. The
 28 symmetry group of the standard model is:

$$SU_C(3) \times SU_L(2) \times U_Y(1), \quad (2.1)$$

29 where the first factor is related to strong interactions, whose mediators are eight gluons,
 30 while $SU_L(2) \times U_Y(1)$ is the electroweak symmetry group, whose mediators are photons and
 31 Z - W^\pm bosons.

32 In renormalizable theories, with no anomalies, all gauge bosons are expected to be massless,
 33 in contrast with our experimental knowledge. This inconsistency is solved by introducing a
 34 new scalar particle, the Higgs boson, that can give mass to weak bosons and fermions via the
 35 spontaneous symmetry breaking mechanism.

36 In the last decades, Standard Model has been accurately probed by many experimental
 37 facilities (LEP, Tevatron, LHC), and the results lead to an impressive agreement between
 38 theoretical predictions and experiments. The discovery of the Higgs boson at the CERN Large
 39 Hadron Collider, measured by both CMS and ATLAS collaborations [1–7], represents not only
 40 an extraordinary confirmation of the model, but also the latest biggest achievement in particle
 41 physics as a whole.

43 2.1 Beyond Standard Model theories

44 Even though the Standard Model is the most complete picture of the universe of the particles,
 45 many questions are still left open. From a phenomenological point of view, some experimental
 46 observations are not included in the theory:

- 47 • in SM, neutrinos are massless (whilst experimentally their masses are confirmed to be
 48 non-zero, i.e. by the neutrino oscillations);

- 49 • no candidates for dark matter are predicted;
- 50 • no one of the fields included in the SM can explain the cosmological inflation;
- 51 • SM can not justify the matter-antimatter asymmetry.
- 52 From a purely theoretical perspective, some issues are still relevant in the formulation of the
53 model:
- 54 • *Flavour problem.*
55 The Standard Model has 18 free parameters: 9 fermionic masses; 3 angular parameters in
56 Cabibbo-Kobayashi-Maskawa matrix, plus 1 phase parameter; electromagnetic coupling
57 α ; strong coupling α_{strong} ; weak coupling α_{weak} ; Z mass; the mass of the Higgs boson.
58 Such a huge number of degrees of freedom marks the SM as weakly predictive in the
59 flavour sector.
- 60 • *Unification.*
61 There is not a “complete” unification of strong, weak and electromagnetic interactions,
62 since each one has its own coupling constant, behaving differently at different energy
63 scales; not to mention the fact that gravitational interaction is completely excluded from
64 the SM.
- 65 • *Hierarchy problem.*
66 From Quantum Field Theory, it is known that perturbative corrections to the mass of
67 the scalar bosons included in the theory tend to make it increase towards the energy
68 scale at which the considered theory still holds [8]. If the Standard Model is seen as
69 a low-mass approximation of a more general theory valid up to the Planck mass scale
70 (*i.e.*, $\sim 1.2 \times 10^{19}$ GeV), a fine-tuning cancellation of the order of 1 over 10^{34} is needed
71 in order to protect the Higgs mass at the electroweak scale (~ 100 GeV). Such an aston-
72 ishing correction is perceived as very unnatural.
- 73 Numerous Beyond Standard Model theories (BSM) have been proposed in order to over-
74 come the limits of the Standard Model.
- 75 Grand Unified Theories (GUT) aim at extending the symmetry group of the SM (eq. 2) into
76 largest candidates, such as $S0(10)$, $SU(5)$ and $E(6)$. At GUT scale, approximately at 10^{16} GeV,
77 non-gravitational interactions are expected to be ruled by only one coupling constant, α_{GUT} .
- 78 Super Symmetryc (SUSY) models state that every fermion (boson) of the Standard Model has a
79 bosonic (fermionic) superpartner, with exactly the same quantum numbers, except the spin. If
80 SUSY is not broken, each couple of partners and superpartners should have the same masses,
81 hypothesis excluded by the non-observation of the s-electron. Super Symmetry represents a
82 very elegant solution of the hierarchy problem of the Higgs boson mass, since the perturba-
83 tive corrections brought by new SUSY particles exactly cancel out the divergences caused by
84 SM particles corrections. A particular sub-class of SUSY models, Minimal Super Symmetric
85 Standard Models, is characterized by the introduction of a new symmetry, the R-parity, that
86 guarantees the proton stability and also the stability of the lightest SUSY particle, a possible
87 good candidate for dark matter.
- 88
- 89 Two other possible theoretical pictures are extensively described in sec. 2.2-2.3.

90 2.2 Heavy Vector Triplet

91 The heavy vector triplet model [9] provides a general framework aimed at studying new
 92 physics beyond the standard model, that can manifest into the appearance of new resonances.
 93 The adopted approach is that of the simplified model, in which an effective Lagrangian is
 94 introduced, in order to describe the properties and interactions of new particles (in this case,
 95 a triplet of spin-1 bosons) by using a limited set of parameters, that can be easily linked
 96 to the physical observables at the LHC experiments. These parameters can describe many
 97 physical motivated theories (such as sequential extensions of the SM [10, 11] or Composite
 98 Higgs [12, 13]).

99 Since a simplified model is not a complete theory, its validity is restricted to the on-shell
 100 quantities related to the production and decay mechanisms of the new resonances, that is how
 101 most of the LHC BSM searches are performed. Given these conditions, experimental results
 102 in the resonant region are sensitive to a limited number of the phenomenological Lagrangian
 103 parameters (or to a combination of those), whilst the remaining parameters tend to influence
 104 the tail of the distributions.

105 Limits on production cross-section times branching ratio ($\sigma\mathcal{B}$), as a function of the invariant
 106 mass spectrum of the probed resonance, can be extracted from experimental data. Given that
 107 $\sigma\mathcal{B}$ are functions of the simplified model parameters and of the parton luminosities, it is then
 108 possible to interpret the observed limits in the parameter space.

109 2.2.1 Simplified Lagrangian

110 The heavy vector triplet framework assumes the existence of an additional vector triplet, V_μ^a ,
 111 $a = 1, 2, 3$, in which two spin-1 particles are charged and one is neutral:

$$V_\mu^\pm = \frac{V_\mu^1 \mp i V_\mu^2}{\sqrt{2}}; \quad (2.2)$$

$$V_\mu^0 = V_\mu^3.$$

112
 113 The triplet interactions are described by a simplified Lagrangian, that is invariant under SM
 114 gauge and CP symmetry, and accidentally invariant under the custodial symmetry $SU(2)_L \times$
 115 $SU(2)_R$:

$$\begin{aligned} \mathcal{L}_V = & -\frac{1}{4} \left(D_\mu V_\nu^a - D_\nu V_\mu^a \right) \left(D^\mu V^\nu{}^a - D^\nu V^\mu{}^a \right) + \frac{m_V^2}{2} V_\mu^a V^\mu{}^a \\ & + ig_V c_H V_\mu^a \left(H^\dagger \tau^a D^\mu H - D^\mu H^\dagger \tau^a H \right) + \frac{g^2}{g_V} c_F V_\mu^a \sum_f \bar{f}_L \gamma^\mu \tau^a f_L \\ & + \frac{g_V}{2} c_{VVV} \epsilon_{abc} V_\mu^a V_\nu^b (D^\mu V^\nu{}^c - D^\nu V^\mu{}^c) + g_V^2 c_{VVH} V_\mu^a V^\mu{}^a H^\dagger H - \frac{g}{2} c_{VW} \epsilon_{abc} W^{\mu\nu}{}^a V_\mu^b V_\nu^c. \end{aligned} \quad (2.3)$$

116
 117 In the first line of the formula 2.3, V mass and kinematic terms are included, described with
 118 the covariant derivative $D_\mu V_\nu^a = \partial_\mu V_\nu^a + g \epsilon^{abc} W_\mu^b V_\nu^c$, where W_μ^a are the fields of the weak inter-
 119 action and g is the weak gauge coupling. V_μ^a are not mass eigenstates, since they mix with the
 120 electroweak fields after the spontaneous symmetry breaking, therefore m_V isn't the physical

121 mass of the V bosons.
 122 The second line describes the interaction of the triplet with the Higgs field and the SM left-
 123 handed fermions; c_H describes the vertices with the physical Higgs and the three unphysical
 124 Goldstone bosons that, for the Goldstone equivalence theorem, are equivalent to the longitu-
 125 dinal polarization of W and Z bosons at high-energy; hence, c_H is related to the bosonic decays
 126 of the resonances. c_F is the analogous parameter describing the V interaction with fermions,
 127 that can be generalized as a flavour dependent coefficient, once defined $J_F^{\mu a} = \sum_f \bar{f}_L \gamma^\mu \tau^a f_L$:
 128 $c_F V_\mu^a J_F^{\mu a} = c_\ell V_\mu^a J_\ell^{\mu a} + c_q V_\mu^a J_q^{\mu a} + c_3 V_\mu^a J_3^{\mu a}$.
 129 The last part of the equation includes terms that are relevant only in strongly coupled scenar-
 130 ios (see sec. 2.2.2) through the V -W mixing, but it does not include vertices of V with light SM
 131 fields, hence it can be neglected while describing the majority of the LHC phenomenology, un-
 132 der the assumptions previously stated. Additional dimension four quadrilinear V interactions
 133 are non relevant for the processes discussed, otherwise their effects would be appreciated in
 134 electroweak precision tests and precise Higgs coupling measurements [14].
 135

136 The parameters in the Lagrangian can be interpreted as follows: g_V describes the strength
 137 of the interaction, that is weighted by c parameters. g_V ranges from $g_V \sim 1$ when the coupling
 138 is weak (sec. 2.2.4), to $g_V \sim 4\pi$ when the coupling is strong (sec. 2.2.5). c parameters are
 139 expected to be $c \sim 1$, except to c_H , that can be smaller for weak couplings. The combinations
 140 describing the vertices, $g_V c_H$ and $g^2/g_V c_F$, can be considered as the fundamental parameters,
 141 used to interpret the experimental results.

142 2.2.2 Mass eigenstates, mixing parameters and decay widths

143 The newly introduced $SU(2)_L$ triplet is expected to mix with the weak SM fields. The $U(1)_{em}$
 144 symmetry is left unbroken by the new interaction, hence the massless combination of the
 145 electroweak fields, namely the photon, is the same as the SM:

$$A_\mu = B_\mu \cos \theta_W + W_\mu^3 \sin \theta_W, \quad (2.4)$$

146 with the usual definitions of the electroweak parameters:

$$\begin{aligned} \tan \theta_W &= \frac{g'}{g} \\ e &= \frac{gg'}{\sqrt{g^2 + g'^2}} \\ g &= e / \sin \theta_w \\ g' &= e / \cos \theta_w. \end{aligned} \quad (2.5)$$

147 The Z boson, on the other hand, mixes with the neutral component of the triplet, V^0 , with
 148 a rotation parametrized with the angle θ_N :

$$\begin{pmatrix} \cos \theta_N & \sin \theta_N \\ -\sin \theta_N & \cos \theta_N \end{pmatrix} \begin{pmatrix} Z \\ V^0 \end{pmatrix}. \quad (2.6)$$

149 The mass matrix of the rotated system is given by:

$$\mathbb{M}_N^2 = \begin{pmatrix} \hat{m}_Z^2 & c_H \zeta \hat{m}_Z \hat{m}_V \\ c_H \zeta \hat{m}_Z \hat{m}_V & \hat{m}_V^2 \end{pmatrix}, \quad (2.7)$$

2.2 Heavy Vector Triplet

150 where the parameters are defined as:

$$\begin{cases} \hat{m}_Z = \frac{e}{2 \sin \theta_W \cos \theta_W} \hat{v} \\ \hat{m}_V^2 = m_V^2 + g_V^2 c_{VVHH} \hat{v}^2 \\ \zeta = \frac{g_V \hat{v}}{2 \hat{m}_V} \\ \frac{\hat{v}^2}{2} = \langle H^\dagger H \rangle \end{cases}, \quad (2.8)$$

151 and \hat{v} , the vacuum expectation value of the Higgs field, can be different from the SM $v = 246$
152 GeV. The physical masses of Z and V^0 , m_Z and M_0 , and θ_N come from the matrix relations:

$$\begin{aligned} \text{Tr}(\mathbb{M}_N^2) &= \hat{m}_Z^2 + \hat{m}_V^2 = m_Z^2 + M_0^2 \\ \|\mathbb{M}_N^2\| &= \hat{m}_Z^2 + \hat{m}_V^2 (1 - c_H^2 \zeta^2) = m_Z^2 M_0^2 \\ \tan 2\theta_N &= \frac{2c_H \zeta \hat{m}_Z \hat{m}_V}{\hat{m}_V^2 - \hat{m}_Z^2}. \end{aligned} \quad (2.9)$$

153 The W^\pm bosons mix with the charged components of the triplet, V^\pm , leading to a mass
154 matrix analogous to eq. 2.10:

$$\mathbb{M}_C^2 = \begin{pmatrix} \hat{m}_W^2 & c_H \zeta \hat{m}_W \hat{m}_V \\ c_H \zeta \hat{m}_W \hat{m}_V & \hat{m}_V^2 \end{pmatrix}, \quad (2.10)$$

155 where \hat{m}_W is defined as:

$$\begin{cases} \hat{m}_W = \frac{e}{2 \sin \theta_W} \hat{v} = \hat{m}_Z \cos \theta_W \end{cases}; \quad (2.11)$$

156 the physical masses of W and V^\pm , m_W and M_\pm , and the angle θ_C parametrizing the rotation
157 of the charged sector are described by:

$$\begin{aligned} \text{Tr}(\mathbb{M}_C^2) &= \hat{m}_W^2 + \hat{m}_V^2 = m_W^2 + M_\pm^2 \\ \|\mathbb{M}_C^2\| &= \hat{m}_W^2 + \hat{m}_V^2 (1 - c_H^2 \zeta^2) = m_W^2 M_\pm^2 \\ \tan 2\theta_C &= \frac{2c_H \zeta \hat{m}_W \hat{m}_V}{\hat{m}_V^2 - \hat{m}_W^2}. \end{aligned} \quad (2.12)$$

158 The custodial symmetry of eq. 2.3 guarantees that:

$$\mathbb{M}_C^2 = \begin{pmatrix} \cos \theta_W & 0 \\ 0 & 1 \end{pmatrix} \mathbb{M}_N^2 \begin{pmatrix} \cos \theta_W & 0 \\ 0 & 1 \end{pmatrix}. \quad (2.13)$$

159

160 By taking the determinant of these matrices, a custodial relation among the masses can be
161 extracted:

$$m_W^2 M_\pm^2 = \cos \theta_W m_Z^2 M_0^2, \quad (2.14)$$

162 that has some very important consequences.

163 Given that this model aims at searching new particles in the TeV scale and that the scale of
164 the electroweak interactions must lay at ~ 100 GeV, a hierarchy of the physical masses seems
165 very natural:

$$\frac{\hat{m}_{(W,Z)}}{\hat{m}_V} \sim \frac{m_{(W,Z)}}{M_{(\pm,0)}} \ll 1; \quad (2.15)$$

¹⁶⁶ ζ parameter can be $\zeta \ll 1$ (weakly coupled scenario) or $\zeta \sim 1$ (strongly coupled scenario).
¹⁶⁷ When eq. 2.15 applies, the second lines in eq. 2.9 and eq. 2.12 can be approximated as follows:

¹⁶⁸

$$\begin{aligned} m_Z^2 &= \hat{m}_Z^2 (1 - c_H^2 \zeta^2) (1 + \mathcal{O}(\hat{m}_Z^2 / \hat{m}_V^2)) \\ m_W^2 &= \hat{m}_W^2 (1 - c_H^2 \zeta^2) (1 + \mathcal{O}(\hat{m}_W^2 / \hat{m}_V^2)). \end{aligned} \quad (2.16)$$

¹⁶⁹
¹⁷⁰ From eq. 2.11, the ratio of the physical masses of the charged and neutral electroweak bosons
¹⁷¹ can be approximated as:

$$\frac{m_W^2}{m_Z^2} \approx \cos \theta_W^2, \quad (2.17)$$

¹⁷² that satisfies the SM tree-level relation $\rho = 1$ if $\cos \theta_W^2 \approx 1. - 0.23$. Adding this approximation
¹⁷³ into eq. 2.14, the V bosons are expected to have the same masses, hence the same production
¹⁷⁴ rates:

$$M_{\pm}^2 = M_0^2 (1 + \mathcal{O}(%)). \quad (2.18)$$

¹⁷⁵ The degenerate mass of the triplet will be called $M_V \approx M_{\pm} \approx M_0$; given 2.15, $M_V = \hat{m}_V$.
¹⁷⁶ Another consequence of the mass hierarchy (2.15) is that the mixing angles $\theta_{(N,C)}$ between the
¹⁷⁷ electroweak fields and the triplet are small:

$$\theta_{(N,C)} \approx c_H \zeta \frac{\hat{m}_{(W,Z)}}{\hat{m}_V} \ll 1, \quad (2.19)$$

¹⁷⁸ hence the couplings among SM particles are very close to the couplings predicted by the SM.

¹⁷⁹ Decay widths into fermions

¹⁸⁰ The couplings among the triplet and SM fermions are expressed as a function of the rotation
¹⁸¹ angles $\theta_{(C,N)}$ and SM couplings (omitting the CKM matrix elements for quarks):

$$\begin{cases} g_L^N = \frac{g^2}{g_V^2} \frac{c_F}{2} \cos \theta_N + (g_L^Z)_{SM} \sin \theta_N \approx \frac{g^2}{g_V^2} \frac{c_F}{2}, \\ g_R^N = (g_R^Z)_{SM} \sin \theta_N \approx 0 \\ g_L^C = \frac{g^2}{g_V^2} \frac{c_F}{2} \cos \theta_C + (g_L^W)_{SM} \sin \theta_N \approx \frac{g^2}{g_V^2} \frac{c_F}{2}, \\ g_R^C = 0 \end{cases}, \quad (2.20)$$

¹⁸² where $g_L^W = g/\sqrt{2}$; $g_{L,R}^{W,Z}$ are those predicted by the standard model. The V bosons interact
¹⁸³ with SM left fermions, and the strength of the couplings with fermions is determined by
¹⁸⁴ $g^2/g_V c_F$, as stated in sec. 2.2.1. The decay width into fermions is then given by:

$$\Gamma_{V^{\pm} \rightarrow f\bar{f}'} \approx 2\Gamma_{V^0 \rightarrow f\bar{f}} \approx N_c \left(\frac{g^2 c_F}{g_V} \right)^2 \frac{M_V}{48\pi}, \quad (2.21)$$

¹⁸⁵ where N_c is the number of colours (3 for quarks, 1 for leptons).

2.2 Heavy Vector Triplet

186 Decay widths into bosons

187 As a starting point, a proper choice of the gauge makes the derivation of the approximate
 188 decay widths easier. While the unitary gauge is very convenient in discussing the electroweak
 189 symmetry breaking mechanism, since it provides a basis in which the Goldstone components
 190 of the scalar fields of the theory are set to zero, it does not properly describe the longitudinally
 191 polarized bosons in high-energy regimes, since it introduces a dependence of the type E/m in
 192 the longitudinal polarization vector, not corresponding to the experimental results. This patho-
 193 logical behaviour can be overcome profiting of the equivalence theorem: while calculating
 194 the scattering amplitude of an high-energy process, the longitudinally polarized vectors are
 195 equivalent to their corresponding Goldstone scalars. The scattering amplitude can therefore
 196 be calculated with Goldstone diagrams.

197 In the so-called equivalent gauge [15], the Higgs doublet is then parametrized as:

$$H = \begin{pmatrix} i\pi_+ \\ \frac{h+h-i\pi_0}{\sqrt{2}} \end{pmatrix}, \quad (2.22)$$

198 and the Goldstones π_0 and π_+ describe respectively W and Z longitudinal bosons; h is the
 199 physical Higgs boson. Rewriting the simplified Lagrangian 2.3 with 2.22 parametrization,
 200 two terms hold the information of the interaction of the V s with the Goldstones:

$$\mathcal{L}_\pi = \dots + c_H \zeta \hat{m}_V V_\mu^a \partial^\mu \pi^a + \frac{g_V c_H}{2} V_\mu^a \left(\partial^\mu h \pi^a - h \partial^\mu \pi^a + \epsilon^{abc} \pi^b \partial^\mu \pi^c \right) + \dots, \quad (2.23)$$

201 that are ruled by the $c_H g_V$ parameters combination. When ζ parameter is $\zeta \approx 1$, the first term
 202 in eq. 2.23 becomes important, and it is absorbed by a redefinition of the V_μ^a and π^a fields,

$$\begin{aligned} V_\mu^a &\rightarrow V_\mu^a + \frac{c_H \zeta}{\hat{m}_V} \partial_\mu \pi^a \\ \pi^a &\rightarrow \frac{1}{\sqrt{1 - c_H^2 \zeta^2}} \pi^a; \quad c_H^2 \zeta^2 < 1. \end{aligned} \quad (2.24)$$

203 By properly taking into account all the terms of the simplified lagrangian in the equivalent
 204 gauge, the partial widths of the dibosonic decays are ($\hat{m}_V = M_V$):

$$\begin{aligned} \Gamma_{V^0 \rightarrow W_L^+ W_L^-} &\approx \Gamma_{V^\pm \rightarrow W_L^\pm Z_L} \approx \frac{g_V^2 c_H^2 M_V}{192\pi} \frac{(1 + c_H c_{VVV} \zeta^2)^2}{(1 - c_H^2 \zeta^2)^2} = \frac{g_V^2 c_H^2 M_V}{192\pi} (1 + \mathcal{O}(\zeta^2)) \\ \Gamma_{V^0 \rightarrow Z_L h} &\approx \Gamma_{V^\pm \rightarrow W_L^\pm h} \approx \frac{g_V^2 c_H^2 M_V}{192\pi} \frac{(1 - 4c_H c_{VVV} \zeta^2)^2}{(1 - c_H^2 \zeta^2)^2} = \frac{g_V^2 c_H^2 M_V}{192\pi} (1 + \mathcal{O}(\zeta^2)). \end{aligned} \quad (2.25)$$

205 Decays in fermions and bosons: concluding remarks

206 From eq. 2.21-2.25, some important conclusions can be extracted.

- 207 • When ζ parameter is small, all the triplet decays (both in fermions and in dibosons),
 208 branching fractions and productions are completely determined by $g^2 c_F / g_V$, $g_V c_H$, and
 209 the degenerate mass of the triplet M_V ,
- 210 • c_{VVV} , c_{VVHH} , c_{VWW} can be neglected, as long as the interest is focused in narrow reso-
 211 nances.

2.2.3 HVT production

Given the mass scale of the resonances, the production mechanisms expected to be relevant are Drell-Yan (fig. 2.1) and Vector Boson Fusion (VBF) (fig. 2.2).

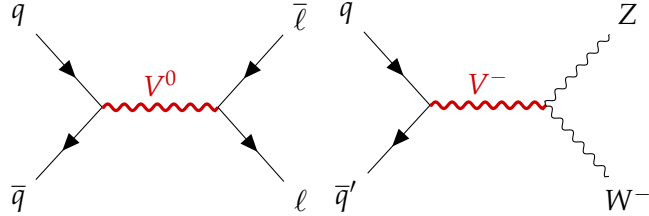


Figure 2.1: Examples of Drell-Yan production mechanism of a heavy V HVT boson: $q - \bar{q}$ quark scattering producing a neutral V^0 that decays leptonically (left); $q - \bar{q}'$ scattering producing a charged V^- that decays in a W and Z bosons (right).

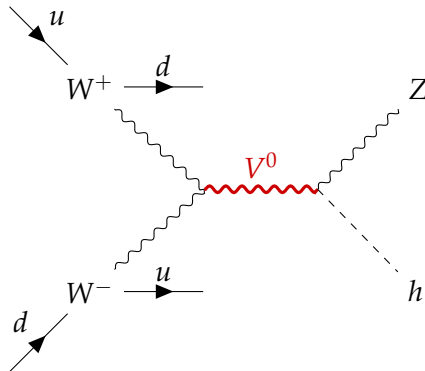


Figure 2.2: Example of VBF production mechanism of a heavy V HVT boson: a neutral V^0 boson is produced by a couple of W bosons, as a result of electroweak interactions of initial state u and d quarks. V^0 decays in a Z boson and a Higgs boson. The final state signature includes the presence of a pair of quarks, due to the primary interactions.

The cross-section of the production mechanisms is given by:

$$\sigma(pp \rightarrow V + X) = \sum_{i,j \in p} \frac{\Gamma_{V \rightarrow ij}}{M_V} f(J, S_i, S_j) g(C_i, C_j) \left. \frac{dL_{ij}}{ds} \right|_{s=M_V^2}, \quad (2.26)$$

where i, j are the partons involved in the hard interaction, Γ_{ij} is the partial width of the process $V \rightarrow ij$, $f(J, S_i, S_j)$ is a function of the spin of the resonance and of the partons, $g(C_i, C_j)$ is a function of the colour factors of each parton, s is the center-of-mass energy and $\frac{dL_{ij}}{ds}$ are the parton luminosities, that are independent from HVT model (that enters only in Γ_{ij}).

Parton luminosities, calculated for a center-of-mass energy of 14 TeV starting from quark and antiquark parton distribution functions (PDF), are displayed in fig. 2.3 (Drell-Yan mechanism) and 2.4 (VBF mechanism). VBF luminosities are suppressed by the α_{EW} factor, therefore the process is relevant only when the bosonic decays of the triplet are dominant (strongly coupled scenario).

2.2 Heavy Vector Triplet

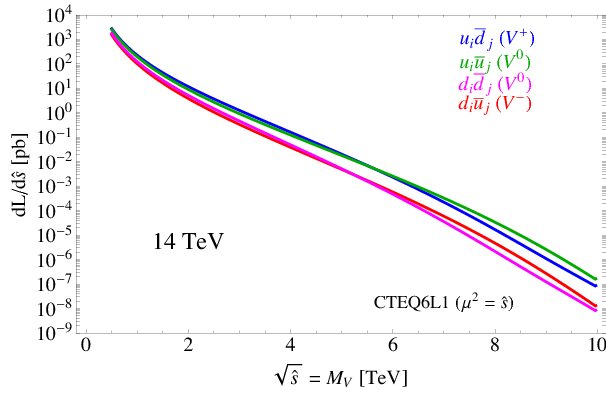


Figure 2.3: Parton luminosities for Drell-Yan process between i and j partons, as a function of the parton center-of-mass energy, for the LHC proton-proton collisions performed at 14 TeV.

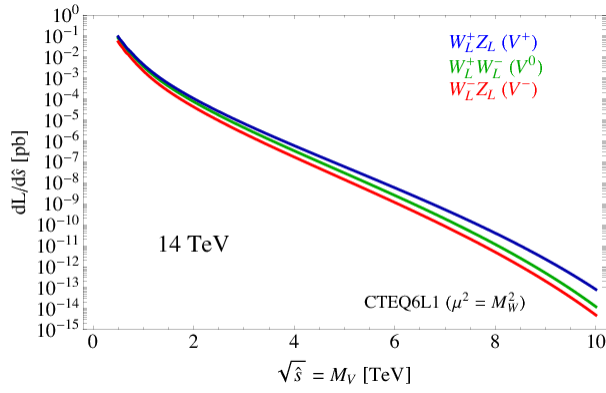


Figure 2.4: Parton luminosities for VBF process between i and j partons, as a function of the parton center-of-mass energy, for the LHC proton-proton collisions performed at 14 TeV.

225 **2.2.4 Benchmark model A: weak coupling scenario**

226 Model A scenario aims at reproducing a simple generalization of the SM [10], obtained by ex-
227 tending the gauge symmetry group with an additional $SU(2)'$. The low-energy phenomena
228 are expected to be dominated by the SM, while the high-energy processes are relevant for the
229 additional symmetry, bringing additional light vector bosons in play.
230 It can be shown that this kind of picture is portrayed by HVT when $c_H \sim -g^2/g_V^2$ and $c_F \sim 1$.
231 This implies that:

$$\begin{aligned} g_V c_H &\approx g^2/g_V \\ g^2 c_F/g_V &\approx g^2/g_V, \end{aligned} \tag{2.27}$$

232 hence the partial decay widths into fermions (eq. 2.21) and bosons (eq. 2.25) differ only by a
233 factor 2 and the colour factor (N_c). Branching fractions for the model A benchmark scenario
234 ($g_V = 1$) are shown in fig. 2.5 (left); total widths are reported in fig. 2.5 (right) for different
235 coupling parameters g_V .

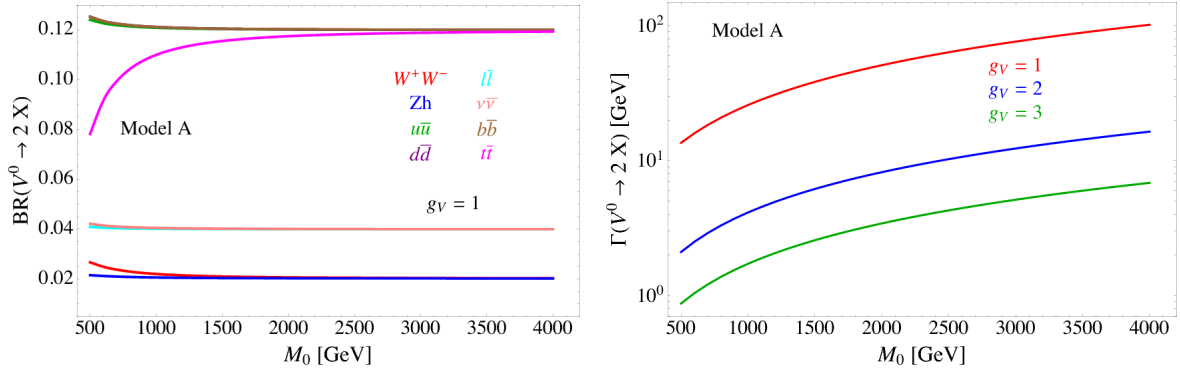


Figure 2.5: HVT model A scenario: branching fractions for fermionic and bosonic decays when $g_V = 1$ (left) as a function of the mass of the resonance M_0 ; total width of the resonance, as a function of its mass, considering different values of the parameter g_V (right).

2.2.5 Benchmark model B: strong coupling scenario

In composite Higgs models [12], the Higgs boson is the result of the spontaneous symmetry breaking of an $SO(5)$ symmetry to a $SO(4)$ group. New vector bosons are expected to appear, and the lightest ones can be represented by HVT model B when $c_H \sim c_F \sim 1$.

In this case:

$$\begin{aligned} g_V c_H &\approx -g_V \\ g^2 c_F / g_V &\approx g^2 / g_V, \end{aligned} \quad (2.28)$$

hence the decay into bosons is not suppressed by g_V parameter. In the benchmark scenario $g_V = 3$, decays into dibosons are largely dominant, as it can be seen in fig. 2.6 (left); the total decay width increases for larger g_V (fig. 2.6, right). When the resonances start to be very broad, *i.e.* $\Gamma / M_V \gg 0.1$, the assumptions leading to the simplified model are no longer valid, hence higher order, non-resonant effects must be taken into account.

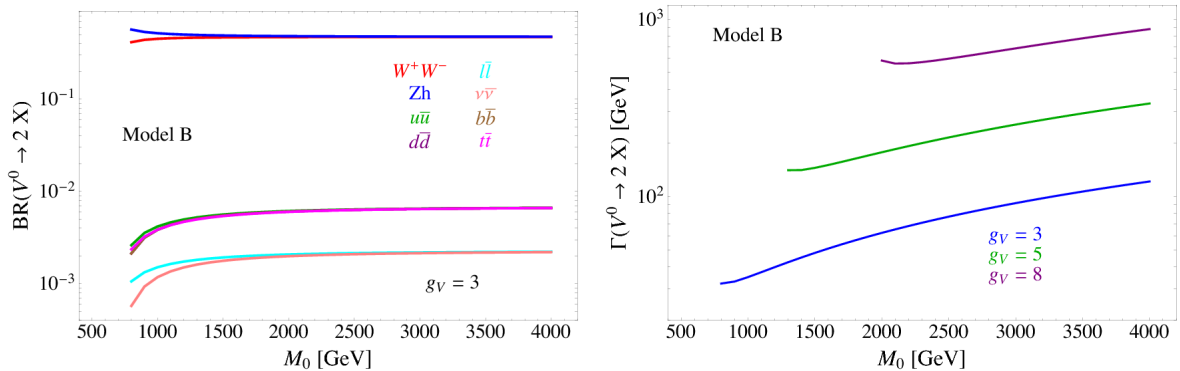


Figure 2.6: HVT model B scenario: branching fractions for fermionic and bosonic decays when $g_V = 3$ (left) as a function of the mass of the resonance M_0 ; total width of the resonance, as a function of its mass, considering different values of the parameter g_V (right).

2.2 Heavy Vector Triplet

2.2.6 Search for HVT resonances at LHC

No evidence of HVT resonances has been observed so far at LHC experiments. Data collected by ATLAS and CMS detectors are used to set limits on the HVT resonance masses and coupling parameters. Experimental results from proton-proton collisions performed at a center-of-mass energy of 8 TeV (Run 1 era) at LHC brought to the following conclusions. A weakly coupled resonance, in the context of benchmark model A ($g_V = 1$) was excluded up to 3 TeV by Run 1 data. By looking at parton luminosities in fig.2.3, in data produced by LHC proton-proton collision at 14 TeV, collected for an integrated luminosity of 300 fb^{-1} , the sensitivity is expected to increase up to $m_V \approx 6 \text{ TeV}$. A strongly coupled resonance, in the context of benchmark model B ($g_V = 3$) is excluded up to 2 TeV by Run 1 data. Data produced by LHC at 14 TeV should increase the sensitivity up to $m_V \approx 3 - 4 \text{ TeV}$. The most stringent limits are provided by the latest data produced by LHC at a center-of-mass energy of 13 TeV (Run 2 era).

Numerous searches for HVT triplet have been performed at CMS experiment in different final states: the most sensitive ones were those in all-hadronic topology. [16, 17] (search for WW , WZ , ZZ resonances in the $q\bar{q}q\bar{q}$ final state) excludes a W' with mass below 3.6 and a Z' with mass below 2.7 TeV in the model B scenario (fig. 2.7). [18, 19] (search for WH , ZH resonances in the $q\bar{q}b\bar{b}$ final state) excludes a W' lighter than 2.97 (3.15) TeV in the HVT model A (model B), and a Z' up to 1.67 (2.26) TeV in HVT model A (model B) (fig. 2.8). In fig. 2.9, results of [16, 17] (left) and [18, 19] (right) searches are interpreted as exclusion contours in the coupling parameter plane of the HVT model ($g_V c_H$ and $g^2 c_F / g_V$). In the grey shaded area, the narrow width approximation fails. The colored curves display the parameter exclusion for different mass hypotheses of the triplet. Colored dots show the model A and B benchmark scenarios.

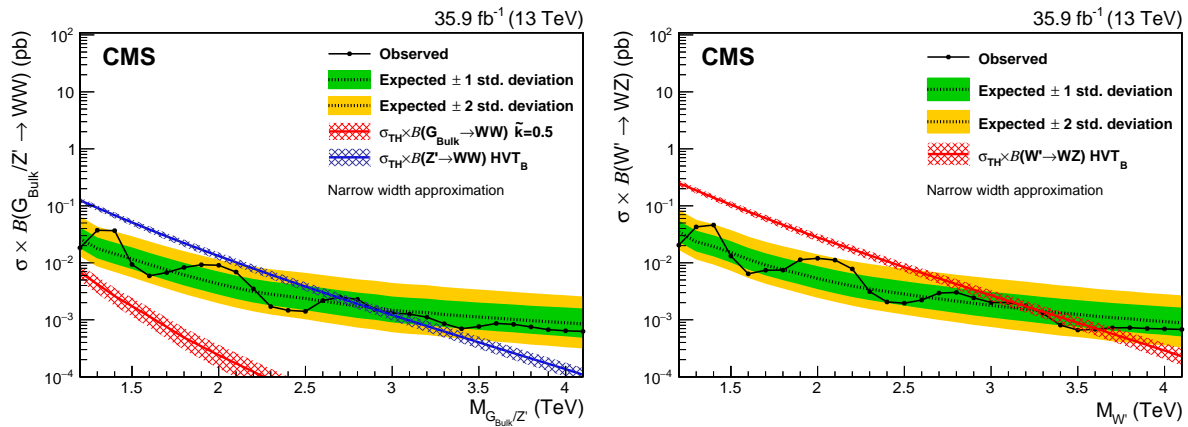


Figure 2.7: The observed and expected limits, with 68% and 95% uncertainty bands, on the product of the cross section and branching fraction $\sigma \mathcal{B}(Z' \rightarrow WW)$ for a spin-1 Z' (left) and $\sigma \mathcal{B}(W' \rightarrow WZ)$ for a spin-1 W' (right), as a function of the reconstructed mass of the diboson resonance. The colored lines show the theoretical predictions for the HVT model B.

Many other final states have been exploited at CMS: $ZW, ZZ \rightarrow \ell\bar{\ell}q\bar{q}$ [20]; $WH, ZH \rightarrow (\ell\bar{\ell}, \ell\nu, \nu\bar{\nu})b\bar{b}$ [21]; $WZ, WW \rightarrow \ell\nu q\bar{q}$ [22]. Finally, $ZW, ZZ \rightarrow \nu\bar{\nu}q\bar{q}$ [23] results will be extensively described in this thesis.

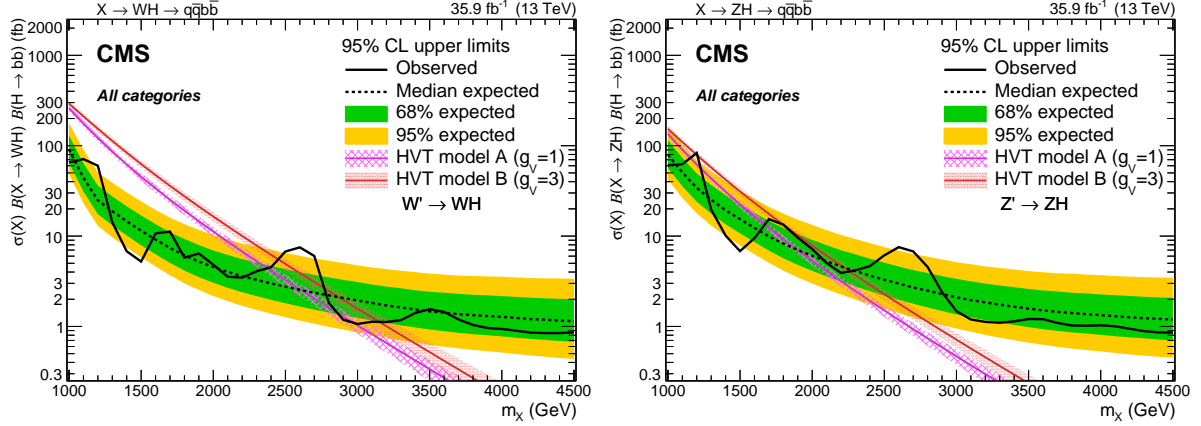


Figure 2.8: The observed and expected limits, with 68% and 95% uncertainty bands, on the product of the cross section and branching fraction $\sigma\mathcal{B}(W' \rightarrow WH)$ for a spin-1 W' (left) and $\sigma\mathcal{B}(Z' \rightarrow ZH)$ for a spin-1 Z' (right), as a function of the reconstructed mass of the diboson resonance. The colored lines show the theoretical predictions for the HVT model A and B.

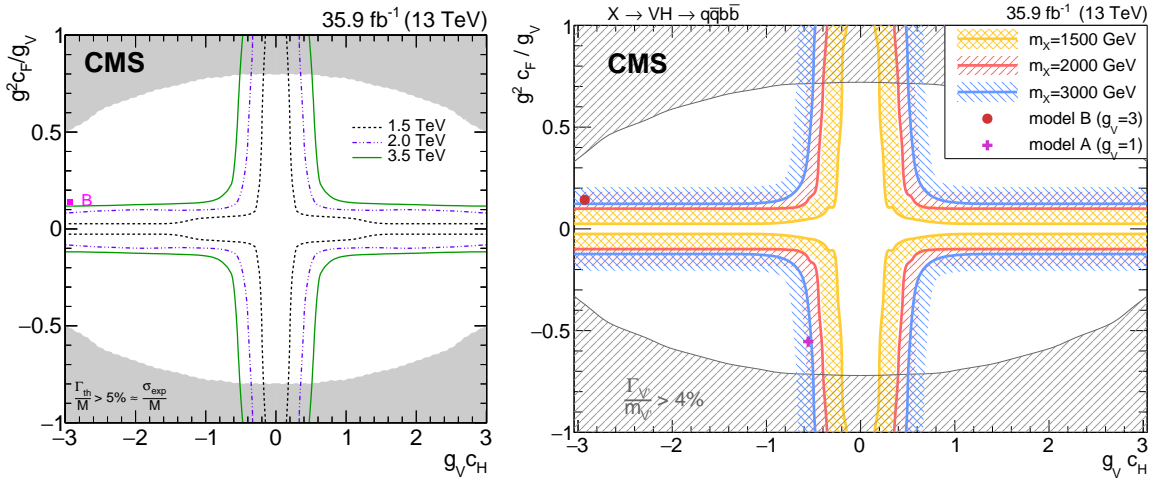


Figure 2.9: Exclusion contours in the coupling parameter plane of the HVT model ($g_V c_H$ and $g^2 c_F / g_V$).

2.2 Heavy Vector Triplet

273 Searches for HVT model B resonances have been performed at ATLAS experiment as well.
 274 Results for a $W' \rightarrow WZ$ reported in fig. 2.10 include the searches performed in $WW, WZ, ZZ \rightarrow$
 275 $q\bar{q}q\bar{q}$ final state [24]; $WZ, WW \rightarrow \ell\nu q\bar{q}$ final state [25]; $ZW, ZZ \rightarrow (\ell\bar{\ell}, \ell\nu, \nu\bar{\nu})q\bar{q}$ final state [26].
 276 The all-hadronic final state has the best sensitivity and it excludes a W' resonance up to 3.3
 277 TeV (model B scenario). Results for a $W' \rightarrow WH$ and for a $Z' \rightarrow ZH$ are displayed in fig. 2.11
 278 (left and right respectively), and they include searches performed in $WH, ZH \rightarrow q\bar{q}b\bar{b}$ final
 279 state [27], and $WH, ZH \rightarrow \ell\bar{\ell}, \ell\nu, \nu\bar{\nu} b\bar{b}$ [28]. A W' is excluded up to 2.9 TeV and a Z' is
 280 excluded up to 2.8 TeV (in the model B scenario).

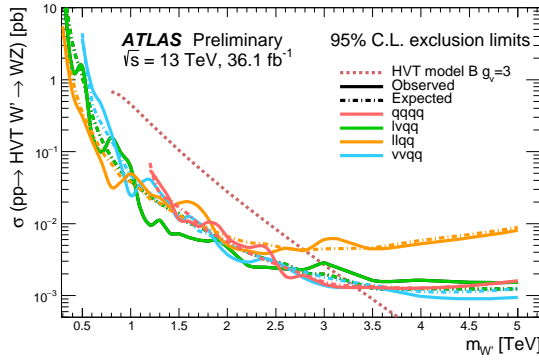


Figure 2.10: The observed and expected limits on the product of the cross section and branching fraction $\sigma\mathcal{B}(W' \rightarrow WZ)$ for a spin-1 W' , as a function of the reconstructed mass of the diboson resonance. The dotted line shows the theoretical predictions for the HVT model B.

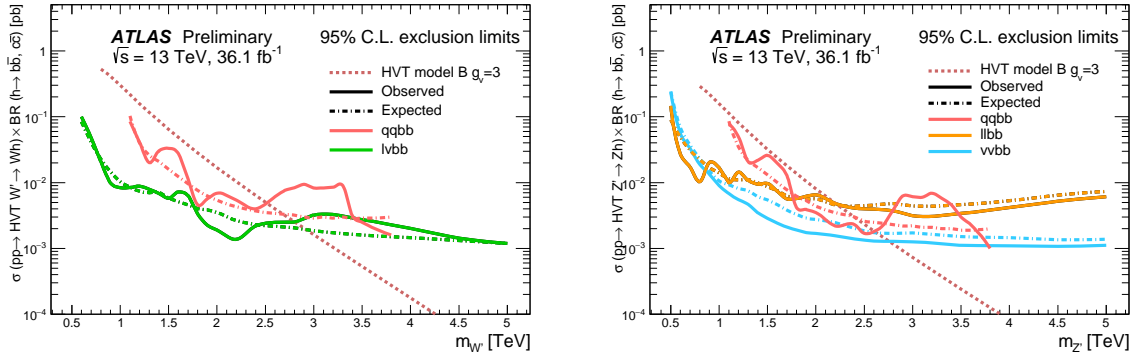


Figure 2.11: The observed and expected limits on the product of the cross section and branching fraction $\sigma\mathcal{B}(W' \rightarrow WH)$ for a spin-1 W' (left) and $\sigma\mathcal{B}(Z' \rightarrow ZH)$ for a spin-1 Z' (right), as a function of the reconstructed mass of the diboson resonance. The colored lines show the theoretical predictions for the HVT model B.

²⁸¹ **2.3 Warped extra dimension**

²⁸² The Randall-Sundrum model [29,30] (RS1) proposes the introduction of one additional warped
 283 dimension in order to solve the hierarchy problem. The metric of the 5-dimensional space (a
 284 slice of AdS_5) generates an exponential hierarchy between the electroweak and Planck scales,
 285 associated respectively to the TeV three-brane, where the SM particles are confined, and the
 286 Planck three-brane. As a consequence of the new geometry, spin-2 massive gravitons are pre-
 287 dicted to exist.

²⁸⁸ The bulk extension of the Randall-Sundrum model [31,32] states that the SM fields can prop-
 289 agate in the extra dimension. Light fermions are near the Planck brane, heavy fermions are
 290 close to the TeV brane, while the Higgs sector is confined in the TeV brane. Higgs couplings
 291 to the heavy fermions are therefore expected to be stronger: this naturally arising hierarchy
 292 of the masses of the SM fields gives a solution to the flavour problem. In this scenario, the
 293 fermionic decays of the bulk gravitons are suppressed, while the bosonic decays are preferred.

²⁹⁴ **2.3.1 Randall-Sundrum original model (RS1)**

²⁹⁵ The existence of additional n -dimensions implies that the effective Planck scale observed in
 296 4-dimensions, $M_{PL} = 1.220910^{19}$ GeV, is related to the fundamental $4+n$ -dimensional Planck
 297 scale, M , via the geometry. M is expected to be of the order of the reduced $\overline{M}_{PL} = M_{PL}/2\pi$.
 298 If the 4-dimensional and the n additional metrics are factorizable, \overline{M}_{PL} is the product of M
 299 and the volume of the compact space V_n :

$$\overline{M}_{PL}^2 = V_n M^{2+n}. \quad (2.29)$$

³⁰⁰ If $M \sim$ TeV, this implies that V_n must be very large, hence the compactification scale $\mu \sim 1/V_n^{1/n}$
 301 is small (eV – MeV for n=2 – 7). Given the smallness of μ when compared to the electroweak
 302 scale, the effects of the extra dimensions should be evident in SM processes. Since they are
 303 not observed, SM particles are assumed to be confined in a 4-dimensional space, the TeV
 304 three-brane, while only gravity is allowed to propagate into the $4+n$ -dimensional space, the
 305 bulk. This mechanism solves the hierarchy of the Higgs scale but introduces a new hierarchy
 306 between μ and M .

³⁰⁷ In the Randall-Sundrum model [29, 30], only one additional dimension is added. The ge-
 308 ometry of the 5-dimensional bulk is non-factorizable, and it is a slice of AdS_5 spacetime.¹
 309 The 4-dimensional metric is multiplied by an exponential function of the fifth dimension (the
 310 "warp" factor):

$$ds^2 = e^{-2kr_c\phi} \eta_{\mu\nu} dx^\mu dx^\nu + r_c^2 d\phi^2; \quad (2.30)$$

³¹¹ x^μ are the usual 4-dimensional coordinates, $\eta_{\mu\nu} = diag(-1, 1, 1, 1)$ is the Minkowski metric, k
 312 is a scale of order of \overline{M}_{PL} , ϕ is the coordinate of the extra dimension, $0 < |\phi| < \pi$, and r_c is
 313 the compactification radius of this finite interval. 4-dimensional mass scales are obtained by
 314 multiplying the bulk masses by $e^{-2kr_c\phi}$: given the exponential form of the warp factor, a small
 315 r_c suffices for generating a large hierarchy between Planck and Higgs scales.

³¹⁶ Two 4-dimensional three-branes are located at the boundaries of the fifth dimension: the
 317 visible brane at $\phi = \pi$; the hidden brane at $\phi = 0$, and their metrics are obtained starting from

¹An n -dimensional anti-de Sitter space (AdS_n) is a maximally symmetric Lorentzian manifold, that solves the Einstein equation with a negative curvature (negative cosmological constant).

2.3 Warped extra dimension

³¹⁸ the bulk 5-dimensional metric G_{MN} , where $M, N = \mu, \phi$:

$$\begin{aligned} g_{\mu\nu}^{\text{vis}}(x^\mu) &= G_{\mu\nu}(x^\mu, \phi = \pi) \\ g_{\mu\nu}^{\text{hid}}(x^\mu) &= G_{\mu\nu}(x^\mu, \phi = 0). \end{aligned} \quad (2.31)$$

³¹⁹ The classical action is given by:

$$\begin{aligned} S &= S_{\text{gravity}} + S_{\text{vis}} + S_{\text{hid}} \\ S_{\text{gravity}} &= \int d^4x \int_{-\pi}^{+\pi} d\phi \sqrt{-G} (-\Lambda + 2M^3\mathcal{R}) \\ S_{\text{vis}} &= \int d^4x \sqrt{-g_{\text{vis}}} (\mathcal{L}_{\text{vis}} - V_{\text{vis}}) \\ S_{\text{hid}} &= \int d^4x \sqrt{-g_{\text{hid}}} (\mathcal{L}_{\text{hid}} - V_{\text{hid}}), \end{aligned} \quad (2.32)$$

³²⁰ where G (g) is the trace of the G_{MN} ($g_{\mu\nu}$) metric, Λ is the cosmological constant in the bulk,
³²¹ \mathcal{R} is the 5-dimensional Ricci scalar, \mathcal{L} and V are the lagrangian and the vacuum energy of the
³²² hidden and visible branes.

³²³ A 5-dimensional metric that preserves the 4-dimensional Poincaré invariance has the form:

$$ds^2 = e^{-2\sigma(\phi)} \eta_{\mu\nu} dx^\mu dx^\nu + r_c^2 d\phi^2. \quad (2.33)$$

³²⁴ The Poincaré invariance guarantees that r_c does not depend on x^μ . Given 2.33, the solution of
³²⁵ the 5-dimensional Einstein's equations simplifies into:

$$\sigma = r_c |\phi| \sqrt{\frac{-\Lambda}{24M^3}}. \quad (2.34)$$

³²⁶ Furthermore, the Poincaré invariance imposes constraints to the vacuum energies and cosmo-
³²⁷ logical constant:

$$\begin{aligned} V_{\text{hid}} &= -V_{\text{vis}} = 24M^3k \\ \Lambda &= -24M^3k^2. \end{aligned} \quad (2.35)$$

³²⁸ The final 5-dimensional metric is then:

$$ds^2 = e^{-2kr_c|\phi|} \eta_{\mu\nu} dx^\mu dx^\nu + r_c^2 d\phi^2. \quad (2.36)$$

³²⁹ A small r_c is considered, so the effects of the fifth dimension on 4-dimensional spacetime
³³⁰ can't be appreciated. A 4-dimensional effective field theory approach is therefore motivated,
³³¹ and its mass parameters are related to the bulk parameters, M , k and r_c . In the Randall-
³³² Sundrum model, SM matter fields are confined in the TeV brane.

³³³ The massless gravitons, the mediators of the gravitational interaction in the effective field
³³⁴ theory, are the zero modes ($h_{\mu\nu}$) of the quantum fluctuations of the classical solution (2.36):

$$ds^2 = e^{-2kT(x)|\phi|} (\eta_{\mu\nu} + h_{\mu\nu}(x)) dx^\mu dx^\nu + T^2(x) d\phi^2, \quad (2.37)$$

³³⁵ where the usual Minkowski metric has been replaced by $\bar{g}_{\mu\nu}(x) = \eta_{\mu\nu} + h_{\mu\nu}$; $h_{\mu\nu}$ are the
³³⁶ tensor fluctuations around the Minkowski space, and represent both the physical graviton in
³³⁷ 4-dimensions and the massless mode of the Kaluza-Klein decomposition of the bulk metric.

³³⁸ r_c is the vacuum expectation value of $T(x)$.

³³⁹ By substituting eq. 2.37 in the classical action 2.32, an effective action can be extracted, and in
³⁴⁰ particular the curvature term holds:

$$S_{\text{eff}} \sim \int d^4x \int_{-\pi}^{+\pi} d\phi 2M^3 r_c e^{-2kr_c|\phi|} \bar{\mathcal{R}} \sqrt{-\bar{g}}, \quad (2.38)$$

³⁴¹ where \bar{g} is the trace of $\bar{g}_{\mu\nu}$ and $\bar{\mathcal{R}}$ is the 4-dimensional Ricci scalar of $\bar{g}_{\mu\nu}$ metric. In this
³⁴² effective 4-dimensional action, the ϕ dependence can be integrated out, and the 4-dimensional
³⁴³ Planck mass can be calculated:

$$\bar{M}_{PL}^2 = M^3 r_c \int_{-\pi}^{+\pi} d\phi e^{-2kr_c|\phi|} = \frac{M^3}{k} \left(1 - e^{-2kr_c\pi}\right). \quad (2.39)$$

³⁴⁴ It can be shown [29] that a field with a fundamental mass parameter m_0 in the bulk manifests
³⁴⁵ in the visible three-brane with a physical mass m :

$$m = e^{-2kr_c\pi} m_0. \quad (2.40)$$

³⁴⁶ Scales $m \sim \text{TeV}$ are generated from $m_0 \sim \bar{M}_{PL}$ if $e^{kr_c\pi} \sim 10^{15}$. This relation stands still when
³⁴⁷ Higgs field is introduced and confined in the visible three-brane:

$$v = e^{-2kr_c\pi} v_0, \quad (2.41)$$

³⁴⁸ where v is the Higgs vacuum expectation value in the TeV brane and v_0 is the 5-dimensional
³⁴⁹ Higgs v.e.v.

³⁵⁰ The hierarchy problem is then solved by the exponential warp factor. The weakness of gravity
³⁵¹ in the TeV three-brane is motivated by the small overlap of the graviton wave function.

³⁵² In order to calculate the mass spectrum of the graviton in the TeV brane, the tensor fluctuations
³⁵³ of the Minkowski metric are expanded into a Kaluza-Klein (KK) tower $h_{\mu\nu}^{(n)}$:

$$h_{\mu\nu}(x, \phi) = \sum_{n=0}^{\infty} h_{\mu\nu}^{(n)}(x) \frac{\chi^{(n)}(\phi)}{\sqrt{r_c}}. \quad (2.42)$$

³⁵⁴ Once a suitable gauge is chosen, i.e. $\eta^{\mu\nu} \partial_\mu h_{\nu\alpha}^{(n)} = \eta^{\mu\nu} h_{\mu\nu}^{(n)} = 0$, the equation of motion of $h_{\mu\nu}^{(n)}$
³⁵⁵ becomes the Klein-Gordon relation, where $m_n^G \geq 0$:

$$\left(\eta^{\mu\nu} \partial_\mu \partial_\nu - (m_n^G)^2 \right) h_{\mu\nu}^{(n)}(x) = 0. \quad (2.43)$$

³⁵⁶ By substituting eq. 2.42 into Einstein's equation, the solutions for $\chi^{(n)}(\phi)$ (commonly called
³⁵⁷ "profiles") are [33,34]:

$$\chi^{(n)}(\phi) = \frac{e^{2\sigma}}{N} \left[J_2(z_n^G) + \alpha_n Y_2(z_n^G) \right], \quad (2.44)$$

³⁵⁸ where J_2 and Y_2 are second order Bessel functions, N is the normalization of the wavefunction,
³⁵⁹ α_n are coefficients and $z_n^G = m_n^G e^{\sigma(\phi)}/k$. m_n^G is the mass of the n -mode, and it depends on the
³⁶⁰ roots of the Bessel functions $z_n^G = (3.83, 7.02, 10.17, 13.32, \dots)$. In the limit $m_n^G/k \ll 1$ and
³⁶¹ $e^{kr_c\pi} \gg 1$:

$$m_n^G = k z_n^G(\pi) e^{-kr_c\pi}. \quad (2.45)$$

2.3 Warped extra dimension

362 The interactions between the graviton KK modes and the matter fields in the TeV brane can be
363 derived from the 4-dimensional effective Lagrangian, once $h_{\mu\nu}$ is replaced by its KK decom-
364 position:

$$\mathcal{L} = -\frac{1}{M_{PL}} T^{\mu\nu}(x) h_{\mu\nu}^{(0)} - \frac{1}{e^{-kr_c\pi} M_{PL}} T^{\mu\nu}(x) \sum_{n=1}^{\infty} h_{\mu\nu}^{(n)}(x); \quad (2.46)$$

365 $T^{\mu\nu}$ is the space energy-momentum tensor of the matter fields. The zero mode of the gravitons
366 coupling is $1/M_{PL}$, while higher order KK modes couplings to all SM fields are suppressed
367 by $e^{-kr_c\pi} M_{PL}$, that is of the order of the TeV scale. Spin-2 KK masses and couplings are hence
368 determined by the TeV scale, or, equivalently, KK gravitons are close to the TeV brane. This
369 implies that KK gravitons can be produced via $q\bar{q}$ or gluon fusion, and that a leptonic decay
370 of the resonance could represent a very clear signal signature.

371 2.3.2 Bulk extension of RS1: graviton production and decays

372 An extension of the original RS1 formulation has been proposed. It states that the usual SM
373 fields are no longer confined in the TeV brane, but they are the zero modes of the correspond-
374 ing 5-dimensional SM fields. If first and second generation fermions are close to the Planck
375 brane, contribution to flavour changing neutral currents by higher-dimensional operators are
376 suppressed. These contributions are excluded by electroweak precision tests, but they were
377 not prevented in original RS1. The second motivation behind the choice is, as mentioned pre-
378 viously, the naturally arising flavour hierarchy: first and second generation quarks have small
379 Yukawa couplings to the Higgs sector, confined in the TeV brane, while top quark and bosons
380 have stronger Yukawa couplings.

381 In this picture, couplings between higher-order KK gravitons and light fermions are strongly
382 suppressed, resulting into a negligible KK gravitons production via $q\bar{q}$, whilst gluon fusion
383 production becomes dominant. KK gravitons decay into top quarks and Higgs bosons are
384 dominant, given that both their profiles are near the TeV brane, while leptonic decays are
385 negligible. Via the equivalence theorem, the Goldstone bosons are equivalent to the longitu-
386 dinally polarized weak bosons, W_L^\pm and Z_L , that have profiles close to the TeV brane. Decays
387 of KK gravitons into weak dibosons (and production in VBF) are comparable to di-top and
388 di-Higgs decays.

389

390 The KK decomposition and the KK mass spectrum of the graviton have already been pre-
391 sented in sec. 2.3.1. The KK decomposition of a massless 5-dimensional gauge field $A_M(x, \phi)$
392 is similarly performed [35]:

$$A_\mu(x, \phi) = \sum_{n=0}^{\infty} A_\mu^{(n)}(x) \frac{\chi_A^{(n)}(\phi)}{\sqrt{r_c}}. \quad (2.47)$$

393 The profiles for the gauge fields are:

$$\chi_A^{(n)}(\phi) = \frac{e^\sigma}{N_A} \left[J_1(z_n^A) + \alpha_n^A Y_1(z_n^A) \right], \quad (2.48)$$

394 where J_1 and Y_1 are first order Bessel functions. Similarly to eq. 2.49, the mass spectrum of
395 the gauge field is:

$$m_n^A = kz_n^A(\pi) e^{-kr_c\pi}; \quad (2.49)$$

³⁹⁶ the first roots of the Bessel functions are $z_n^A = (2.45, 5.57, 8.70, 11.84, \dots)$.

³⁹⁷ The Lagrangian expressing the interaction between the m and n modes of the bulk field F
³⁹⁸ to the q KK gravitons mode G is [35]:

$$\mathcal{L}_{G-F} = \sum_{m,n,q} C_{mnq}^{FFG} \frac{1}{M_{PL}} \eta^{\mu\alpha} \eta^{\nu\beta} h_{\alpha\beta}^{(q)}(x) T_{\mu\nu}^{(m,n)}(x), \quad (2.50)$$

³⁹⁹ C_{mnq}^{FFG} is the overlap integral of the profiles:

$$C_{mnq}^{FFG} = \int \frac{d\phi}{\sqrt{k}} e^{t\sigma} \chi_F^{(m)} \chi_F^{(n)} \chi_G^{(q)}; \quad (2.51)$$

⁴⁰⁰ t depends on the type of field considered.

⁴⁰¹ The coupling between gluons and the q KK graviton mode is given by:

$$C_{00q}^{AAG} = e^{k\pi r_c} \frac{2 [1 - J_0(x_n^G)]}{k\pi r_c (x_n^G)^2 |J_2(x_n^G)|}. \quad (2.52)$$

⁴⁰² Once eq. 2.52 is put in eq. 2.50, the most significant partial decay widths into the q KK graviton
⁴⁰³ mode are:

$$\begin{aligned} \Gamma(G \rightarrow t_R \bar{t}_R) &\sim N_c \frac{[\tilde{k} x_q^G]^2 m_q^G}{320\pi} \\ \Gamma(G \rightarrow hh) &\sim \frac{[\tilde{k} x_q^G]^2 m_q^G}{960\pi} \\ \Gamma(G \rightarrow W_L^+ W_L^-) &\sim \frac{[\tilde{k} x_q^G]^2 m_q^G}{480\pi} \\ \Gamma(G \rightarrow Z_L Z_L) &\sim \frac{[\tilde{k} x_q^G]^2 m_q^G}{960\pi}, \end{aligned} \quad (2.53)$$

⁴⁰⁴ where $\tilde{k} = k/\overline{M}_{PL}$; the total decay width is:

$$\Gamma_G = \frac{13 [\tilde{k} x_q^G]^2 m_q^G}{960\pi}. \quad (2.54)$$

⁴⁰⁵ Calculations, so far, have been performed considering $M \sim \overline{M}_{PL}$ and $k < M$, hypotheses
⁴⁰⁶ under which the solution for the bulk metric (eq. 2.36) is valid. Hence, $\tilde{k} = k/\overline{M}_{PL} \leq 1$ is
⁴⁰⁷ taken as a reference interval. This has also phenomenological consequences on the width of
⁴⁰⁸ the resonance, as stated in eq. 2.54. The total decay width of the lightest KK graviton mode,
⁴⁰⁹ compared to its mass, is shown as a function of \tilde{k} in fig. 2.12 [36]. At $\tilde{k} = 1$, in the bulk
⁴¹⁰ scenario, the KK graviton width is expected to be few % of its mass, up to 4 TeV (dotted red
⁴¹¹ curve). The narrow width approximation holds, hence the resonance properties can be probed
⁴¹² at the peak, neglecting the effects in the tails of the mass distribution.

⁴¹³ The total cross-section of a bulk graviton, produced at LHC in proton-proton interactions
⁴¹⁴ via gluon fusion (displayed in fig. 2.13), decaying into a couple of vector bosons (for the
⁴¹⁵ purpose of this thesis, a final state with two longitudinally polarized Z bosons is considered)

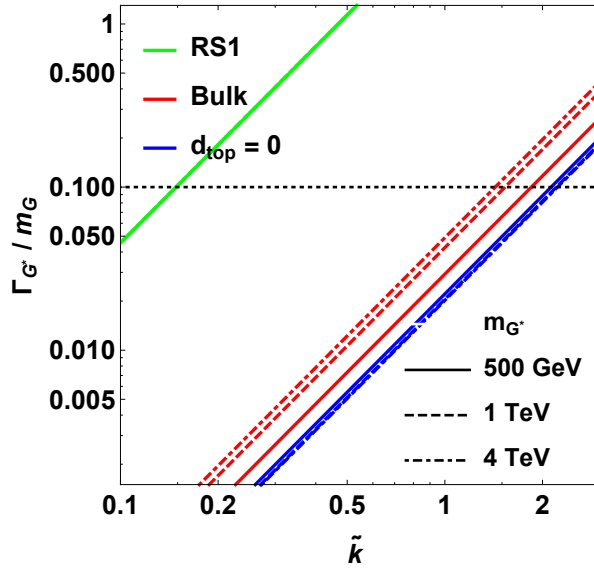


Figure 2.12: Width of the KK gravitons, in units of the mass of the resonance, as a function of the curvature parameter \tilde{k} . The red curves represent the bulk extension of RS1 original model for different mass hypotheses (from 500 GeV up to 4 TeV).

⁴¹⁶ is expressed as a function of the parton level cross-section $\hat{\sigma}$, the gluon parton distribution
⁴¹⁷ functions f_g , the momentum transfer $Q^2 \sim (m_q^G)^2$ and the center-of-mass energy s :

$$\sigma(pp \rightarrow ZZ) = \int dx_1 dx_2 f_g(x_1, Q^2) f_g(x_2, Q^2) \hat{\sigma}(x_1 x_2 s). \quad (2.55)$$

⁴¹⁸ The differential parton level cross-section, averaged over colors and initial spin states, is (hatted
⁴¹⁹ quantities are calculated in the center-of-mass frame):

$$\frac{d\hat{\sigma}(gg \rightarrow ZZ)}{d \cos \hat{\theta}} \approx \frac{|\mathcal{M}_{+-00}|^2}{1024\pi \hat{s}}, \quad (2.56)$$

⁴²⁰ where $|\mathcal{M}_{+-00}|$ is the matrix element of the dominant contribution in $gg \rightarrow VV$ process (Γ_G
⁴²¹ is defined in eq. 2.54, a, b are color factors):

$$\mathcal{M}_{+-00}(g^a g^b \rightarrow VV) = -C_{00q}^{AAG} e^{-k\pi r_c} \left(\frac{x_n^G \tilde{k}}{m_n^G} \right)^2 \sum_n \frac{\delta_{ab} \mathcal{A}_{+-00}}{\hat{s} - m_n^G{}^2 + i\Gamma_G m_n^G}. \quad (2.57)$$

⁴²² The relevant amplitudes taken account in the matrix element calculation are [31]:

$$\mathcal{A}_{+-00} = \mathcal{A}_{-+00} = \frac{(1 - 1/\beta_Z^2) (\beta_Z^2 - 2) [(\hat{t} - \hat{u})^2 - \beta_Z^2 \hat{s}^2] \hat{s}}{8M_Z^2}, \quad (2.58)$$

⁴²³ where $\beta_Z^2 = 1 - 4M_Z^2/\hat{s}$ and M_Z is the mass of the Z boson.

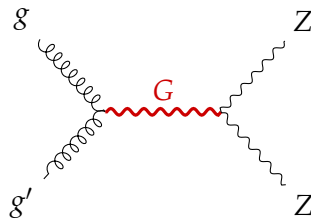


Figure 2.13: Gluon fusion production mechanism for a KK graviton that decays in a couple of Z bosons.

424 2.3.3 Search for KK bulk gravitons at LHC

425 No evidence of spin-2 bulk graviton resonances has been observed so far at LHC experiments.
 426 Data collected by ATLAS and CMS detectors are used to set limits on the graviton masses,
 427 generally considering different curvature parameter \tilde{k} hypotheses, once assured the narrow
 428 width approximation is still valid (up to $\tilde{k} \sim 1$). The most stringent limits have been set with
 429 Run 2 data.

430 Many results of the diboson searches performed at CMS and already presented in sec. 2.2.6
 431 are interpreted in the context of the bulk gravitons, together with the additional final states
 432 $WZ, ZZ \rightarrow \ell\bar{\nu}\ell\bar{\nu}$ [37] and $HH \rightarrow b\bar{b}b\bar{b}$ [38]. The most interesting limit is provided by [37], that,
 433 under the hypothesis $\tilde{k} = 0.5$, excludes a spin-2 bulk graviton with a mass lower than 800 GeV
 434 (fig. 2.14).

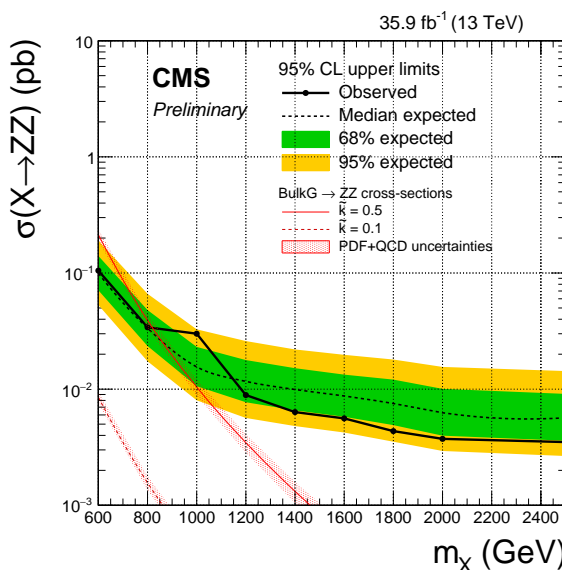


Figure 2.14: The observed and expected limits, with 68% and 95% uncertainty bands, on the product of the cross section and branching fraction $\sigma\mathcal{B}(G \rightarrow ZZ)$ for a spin-2 bulk graviton, as a function of the reconstructed mass of the diboson resonance. The colored lines show the theoretical predictions for $\tilde{k} = 0.1$ and 0.5 .

435 Similarly for ATLAS experiment, searches for diboson resonances in sec. 2.2.6 have been

2.3 Warped extra dimension

⁴³⁶ interpreted in the graviton context. The most stringent limit is given by [25], where, under the
⁴³⁷ assumption $\tilde{k} = 1$, a spin-2 bulk graviton with mass lower than 1.76 TeV is excluded (fig. 2.15).

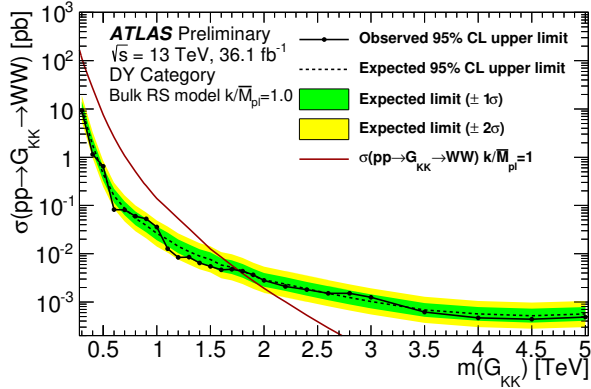


Figure 2.15: The observed and expected limits, with 68% and 95% uncertainty bands, on the product of the cross section and branching fraction $\sigma\mathcal{B}(G \rightarrow ZZ)$ for a spin-2 bulk graviton, as a function of the reconstructed mass of the diboson resonance. The colored lines show the theoretical predictions for $\tilde{k} = 1$.

The Large Hadron Collider and the CMS experiment

3.1 The Large Hadron Collider

441 The Large Hadron Collider (LHC) is a 27 km ring structure designed for the acceleration and
 442 collision of protons and heavy ions. It is situated approximately 100 m underground, be-
 443 tween France and Switzerland, in the Geneva area, and it is the most important of the CERN
 444 (Conseil européen pour la recherche nucléaire) facilities. It has been designed to fit the pre-
 445 existing underground tunnel of the LEP collider [ref. 24 Jacopo], built to accelerate electrons
 446 and positrons until the year 2000, in order to reduce the cost of the project, definitively ap-
 447 proved in 1996.

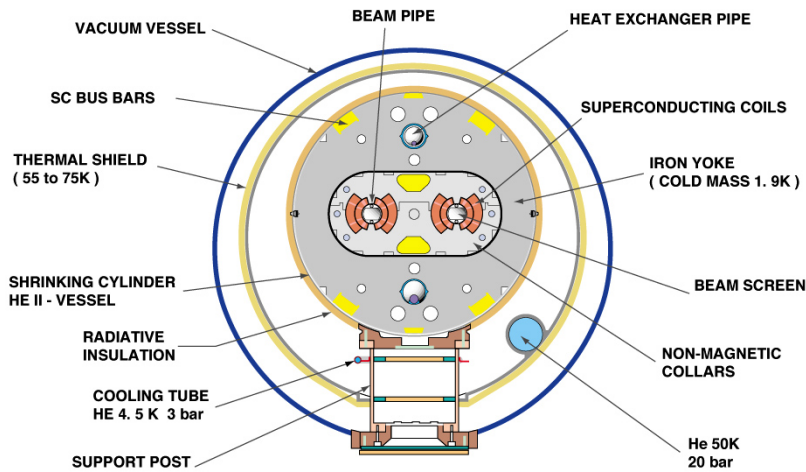
448 Moving from an electron-positron collider to an hadron collider allowed to reach higher ener-
 449 gies in the center-of-mass frame, since the synchrotron radiation loss is inversely proportional
 450 to the fourth power of the mass of the particle involved: hence, it is reduced by a factor
 451 $m_p/m_e \sim 10^3$. Furthermore, at a proton-proton collider it is possible to collect higher lumi-
 452 nosities (and hence more statistics) with regards to, for example, a proton-antiproton collider,
 453 like Tevatron at Fermilab, in the USA.

454 In the LHC two identical beam pipes rings are designed to let protons circulate in opposite
 455 directions, in ultrahigh vacuum conditions (10^{-13} atm) in order to avoid collisions with gas
 456 molecules.

457 LHC è dotato di due anelli identici, entro cui i fasci di particelle corrono in direzioni op-
 458 poste in tubi a vuoto. La geometria di LHC si basa su quella precedente di LEP: l'acceleratore
 459 è diviso in 8 strutture ad arco per la curvatura delle traiettorie e in segmenti lunghi 520 m
 460 utili per l'iniezione e per strumenti di controllo del sistema. I fasci di protoni collidono in 4
 461 punti di interazione, nei quali sono installati i quattro principali rivelatori: ALICE, ATLAS,
 462 CMS, LHCb.

463 Il ridotto diametro interno del tunnel, di circa 4 m, ha comportato delle limitazioni nella
 464 costruzione dei magneti superconduttori, costringendo ad accoppiare magneticamente i due
 465 fasci. In figura ?? è mostrata una sezione delle strutture ad arco. Attorno ai tubi di fascio sono

CROSS SECTION OF LHC DIPOLE



CERN AC _HE107A_ V02/02/98

Figure 3.1: Sezione della struttura ad arco per la curvatura delle traiettorie dei protoni.

467 disposti due magneti dipolari a superconduttore, essi generano due campi magnetici verticali
 468 paralleli e discordi e sono preposti alla curvatura delle traiettorie. Oltre a questi, si trovano
 469 magneti quadrupolari, utili per la focalizzazione dei fasci, e altri piccoli magneti con sei o otto
 470 poli per piccole correzioni sulla dimensione dei fasci e sulla loro posizione. Tutti i magneti e
 471 le cavità acceleratrici sono costruite in metalli (titano e niobio) superconduttori, che vengono
 472 raffreddati a -271.3°C (1.9K) con sistemi ad elio liquido. In LHC ci sono un totale di 1232
 473 magneti dipolari e 392 quadrupolari, capaci di creare un campo magnetico massimo di 8.33 T.
 474 Come detto, LHC è soltanto la fase terminale di una serie di macchine che accelerano i protoni
 475 ad energie crescenti. I protoni vengono estratti da atomi di idrogeno, quindi vengono immessi
 476 in un acceleratore lineare, Linac2, che li porta a 50 MeV. Successivamente vengono accelerati in
 477 un piccolo sincrotrone, un Booster, che ne aumenta l'energia fino a 1.4 GeV, quindi nel Proton
 478 Synchrotron dove arrivano a 25 GeV. Il Super Proton Synchrotron li accelera fino a 450 GeV
 479 ed infine essi vengono iniettati nell'anello principale di LHC, dove le cavità a radiofrequenza
 480 li porteranno, nominalmente, fino a 14 TeV. Uno schema degli apparati di accelerazione e
 481 iniezione è mostrato in figura ??[13].
 482 I fasci, ad LHC, sono suddivisi in pacchetti, necessari per risolvere una delle problematiche che
 483 sorgono ai sincrotroni (detta stabilità di fase). Prima della collisione, speciali magneti riducono
 484 ciascun pacchetto ad una larghezza di $16 \mu\text{m}$ e ad una lunghezza di 80 mm. In ognuno sono
 485 presenti circa 10^{11} protoni. Presso l'esperimento CMS, secondo il progetto di costruzione,
 486 le collisioni avverranno ogni 25 ns (fino ad ora sono avvenute ogni 50 ns), corrispondenti a
 487 una frequenza di 40 MHz e ad una luminosità istantanea di $10^{34} \text{ cm}^{-2}\text{s}^{-1}$. Queste frequenze
 488 elevate generano un problema noto con il nome di "pile-up", che consiste nel moltiplicarsi del
 489 numero di vertici primari di interazione. Ad un medesimo evento registrato prodotto dalle
 490 collisioni ogni 50 ns, infatti, corrispondono fino a 30 vertici di interazione; essi aumenteranno
 491 a 40 quando si arriverà a realizzare una collisione ogni 25 ns.

3.1 The Large Hadron Collider

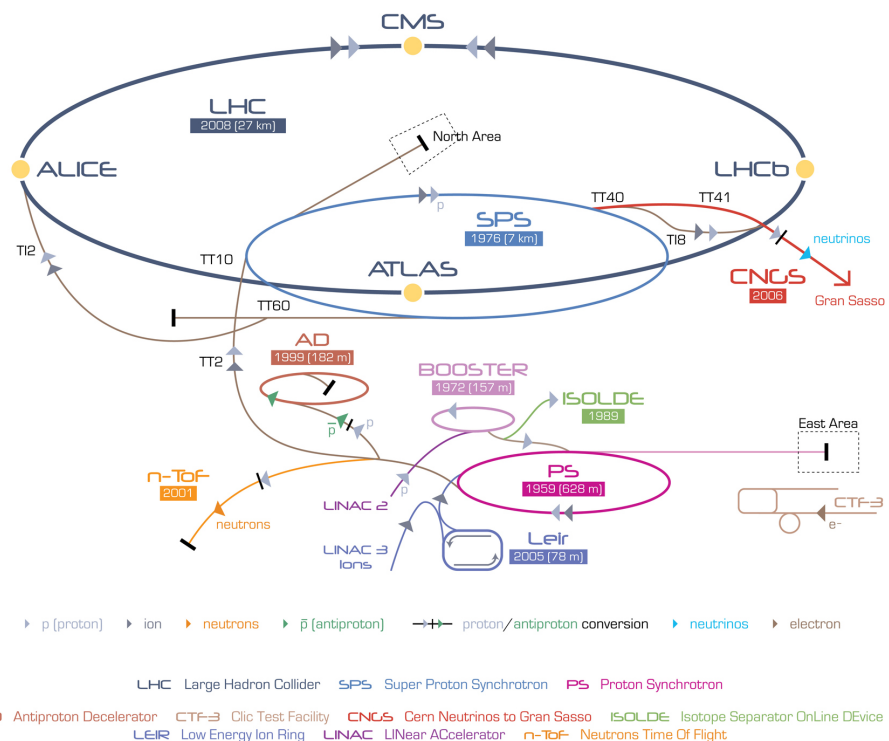


Figure 3.2: Schema dell'apparato di iniezione e rivelazione nel tunnel di LHC. LHC è preposto a molteplici scopi oltre alle collisioni protone-protone, tra cui accelerazione e collisioni tra ioni pesanti (esperimento ALICE), produzione di fasci di neutrini per osservarne le oscillazioni (esperimento CerN to Gran Sasso).

Le quantità di rilevanza per un acceleratore sono l'energia del centro di massa, che definisce la massima energia disponibile negli scontri tra le particelle, corrispondente alla somma delle energie dei singoli fasci, e la luminosità, che descrive invece la frequenza di interazione tra i fasci. Ammettendo che ciascun pacchetto di un fascio contenga n_1 protoni e l'altro ne contenga n_2 , che l'area in cui i pacchetti si urtano sia Σ e che la frequenza di rivoluzione attorno all'anello sia f ,abbiamo che la luminosità istantanea è data da:

$$\mathcal{L} = f \frac{n_1 n_2}{\Sigma}. \quad (3.1)$$

Un generico processo i -esimo con sezione d'urto σ_i avrà allora la frequenza di interazione R_i :

$$R_i = \frac{dN_i}{dt} = \sigma_i \mathcal{L}, \quad (3.2)$$

mentre il numero di eventi totali registrati nell'intervallo di tempo $(0, \tau)$ si ottiene tramite la luminosità integrata:

$$N_i = \sigma_i \int_0^\tau \mathcal{L} dt. \quad (3.3)$$

3.1.1 Interazioni protone-protone

Nonostante la possibilità di raggiungere luminosità ed energie maggiori, le collisioni tra protoni sono molto più complesse rispetto a quelle tra leptoni: non soltanto per la proliferazione

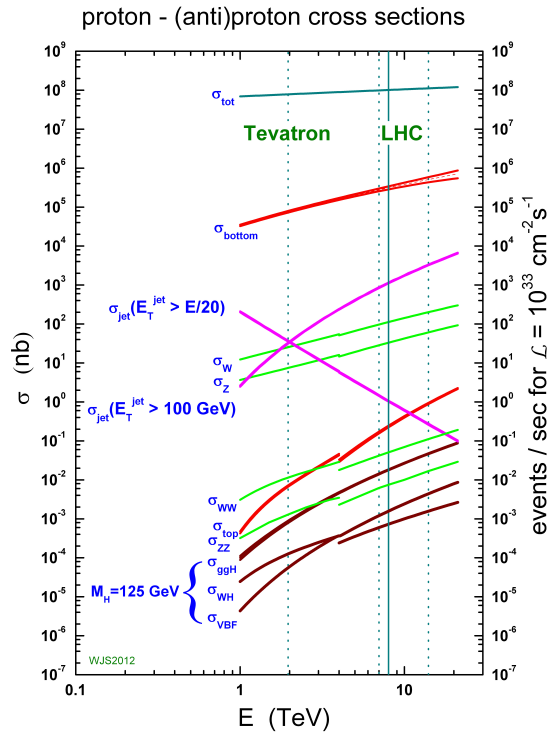


Figure 3.3: Sezioni d’urto e frequenza di eventi attesi da collisioni protone-protone in funzione della massa della particella prodotta (o dell’energia trasversa più alta dei jets prodotti) per $\sqrt{s} = 14 \text{ TeV}$ [14].

504 dei fondi, specialmente da QCD, che rendono molto difficoltoso discriminare il segnale e dis-
 505 tinguere i vertici di interazione primari (il loro moltiplicarsi va sotto il nome di *pileup*), ma
 506 anche per l’impossibilità di conoscere con esattezza l’impulso dei partoni che partecipano alla
 507 collisione.

508 La maggior parte degli eventi ad LHC sono le interazioni soffici, vale a dire con basso mo-
 509 mento trasverso: si tratta tipicamente di urti elasticci o difrattivi che non sono di interesse per
 510 indagini di nuova fisica. Nei processi detti duri, al contrario, la quantità di momento trasferito
 511 è elevata: questi eventi sono i più semplici da distinguere nelle geometrie dei rivelatori e sono
 512 quelli in cui vengono prodotte le particelle più massive.

513 Come è noto dalla QCD, ad alti momenti trasferiti è lecito trattare un protone come un insieme
 514 di partoni, ciascuno dei quali trasporta una frazione x del momento iniziale del fascio e la cui
 515 struttura è descritta dalle parton distribution function (PDF) $f(x, Q^2)$, funzioni della variabile
 516 di Bjorken e del momento trasferito Q^2 . Nel caso in cui l’energia del centro di massa sia
 517 elevata al punto da rendere trascurabili le masse dei singoli oggetti, l’energia effettivamente
 518 disponibile per gli urti tra due partoni 1 e 2 è una quantità incognita, $\sqrt{x_1 x_2 s}$. La sezione
 519 d’urto di un processo partonico generico si può esprimere sfruttando la fattorizzazione lecita
 520 in regime di QCD perturbativa:

$$\sigma = \int dx_1 f_1(x_1, Q^2) \int dx_2 f_2(x_2, Q^2) \sigma_{12}(x_1 p_1, x_2 p_2, Q^2), \quad (3.4)$$

3.2 CMS detector

521 dove σ_{12} indica la sezione d'urto elementare del processo partonico ed f_1, f_2 sono le PDF.
522 In figura ?? sono rappresentate le sezioni d'urto elementari in funzione della massa della
523 particella prodotta: grazie all'elevata luminosità di LHC è possibile osservare fenomeni molto
524 rari mai visti prima, come ad esempio il decadimento del bosone di Higgs in due fotoni o in
525 quattro leptoni, canali nei quali la particella è stata scoperta nel 2012.

526 3.2 CMS detector

527 Compact Muon Solenoid, installato in una caverna sotterranea nei pressi di Cessy, in Francia,
528 è un rivelatore di forma cilindrica, è lungo 22 m, ha un diametro di 15 m, una massa di 12500
529 tonnellate ed è preposto a molteplici scopi. La maggior parte dei processi fisici che si vogliono
530 esplorare hanno basse sezioni d'urto, mentre, come è ben noto, i prodotti delle collisioni tra
531 protoni sono dominati da elevati fondi QCD: CMS è progettato in modo da avere un'elevata
532 capacità di discriminazione degli eventi rari, sfruttando in particolare i canali comprendenti
533 elettroni e muoni, e una grande precisione di misura dei vertici secondari, necessaria per dis-
534tinguere i τ e gli adroni contenenti quark pesanti. L'elevata luminosità nominale di LHC,
535 come accennato, comporta il problema del pile-up: questi effetti possono essere ridotti uti-
536lizzando rivelatori ad elevata granularità. L'occupazione si abbassa segmentando l'apparato
537 in molti sottogruppi di rivelatori, al costo di dover ottenere un'ottima sincronizzazione tra di
538 essi. L'alta frequenza di interazione, inoltre, necessita un'alta risoluzione temporale. Infine,
539 gli elevati livelli di radiazione attorno al vertice richiedono apparati robusti e resistenti.
540 In figura 3.4 è rappresentato uno schema dell'esperimento e dei principali gruppi di rivelato-
541 tori. Prima di passare a descriverne ciascuno nel dettaglio, ponendo particolare attenzione
542 ai tracciatori e al sistema per l'identificazione dei muoni, voglio precisare alcuni termini ri-
543 correnti. Vista la struttura geometrica di CMS, si preferisce chiamare "barrel" la superficie
544 laterale del cilindro, "endcap" le due basi circolari. I rivelatori "forward", disposti oltre gli
545 endcap, servono per coprire un'ulteriore regione geometrica dove la radiazione è più intensa.
546 I rivelatori di traccia al silicio sono spesso chiamati col nome "tracker"; per il calorimetro
547 elettromagnetico si usa la sigla ECAL; per il calorimetro adronico si usa la sigla HCAL; per il
548 trigger di livello 1 si usa la sigla L1 trigger; per il trigger di alto livello si usa la sigla HLT.
549 La figura ?? esemplifica con chiarezza qual è la traiettoria che ciascun tipo di particella, medi-
550 amente, percorre all'interno di CMS.

551 3.2.1 Il sistema di coordinate

552 Il sistema di coordinate, al quale farò spesso riferimento, è orientato nel seguente modo. L'asse
553 x, in direzione radiale, punta verso il centro dell'anello di LHC; l'asse y è verticale e punta
554 verso l'alto; l'asse z è lungo la direzione del fascio. L'angolo azimutale, Φ , giace nel piano xy
555 e si misura a partire dall'asse x; la coordinata radiale in questo piano si indica con r. L'angolo
556 polare θ è definito nel piano rz. La componente del momento trasversa alla direzione del
557 fascio, indicata con p_T , si calcola dalle componenti x ed y. L'energia trasversa è definita da
558 $E_T = E \sin \theta$.

559 È bene introdurre altre due grandezze di comodo utilizzo, la rapidità y e la pseudorapidità
560 η , definite nei modi seguenti in funzione dell'energia della particella E , del suo momento

CMS Detector

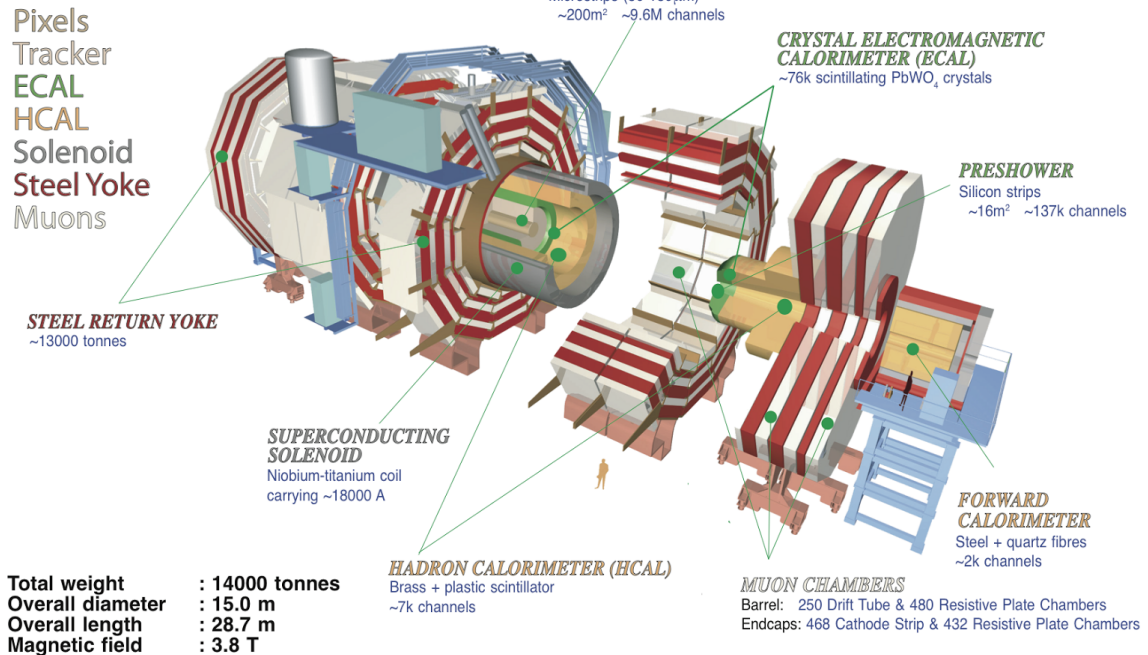


Figure 3.4: Rappresentazione grafica del rivelatore CMS.

561 longitudinale lungo l'asse z e del modulo del momento:

$$y = \frac{1}{2} \log \frac{E + p_z}{E - p_z} \quad (3.5)$$

562

$$\eta = \frac{1}{2} \log \frac{|\vec{p}| + p_z}{|\vec{p}| - p_z} = -\log \tan \frac{\theta}{2}. \quad (3.6)$$

563 Quando la particella è emessa in avanti, ossia per $\theta = 0$, $\eta \rightarrow \infty$. Quando la particella è
 564 emessa trasversalmente al fascio, ossia per $\theta = \pi/2$, $\eta = 0$. Ad energie elevate, quando le
 565 masse diventano trascurabili, rapidità e pseudorapidità coincidono. Queste due grandezze
 566 vengono ampiamente usate perché sono invarianti per boost di Lorentz lungo la direzione del
 567 fascio.

568 3.2.2 Il solenoide

569 Il grande solenoide superconduttore, un cilindro cavo lungo 13 m e di diametro interno pari
 570 a 6 m, fornisce un intenso campo magnetico massimo di 3.8 T, capace di piegare le traiettorie
 571 delle particelle cariche per le misure del loro momento p , data la relazione tra braccio di
 572 leva R e campo magnetico B : $p[\text{GeV}] = 0.3B[\text{T}]R[\text{m}]$. Le linee di campo del magnete sono
 573 chiuse da circa 10000 tonnellate di ferro, che costituiscono il giogo di ritorno intervallato
 574 alle apparecchiature di rivelazione dei muoni. All'interno dei filamenti di niobio e titanio

3.2 CMS detector

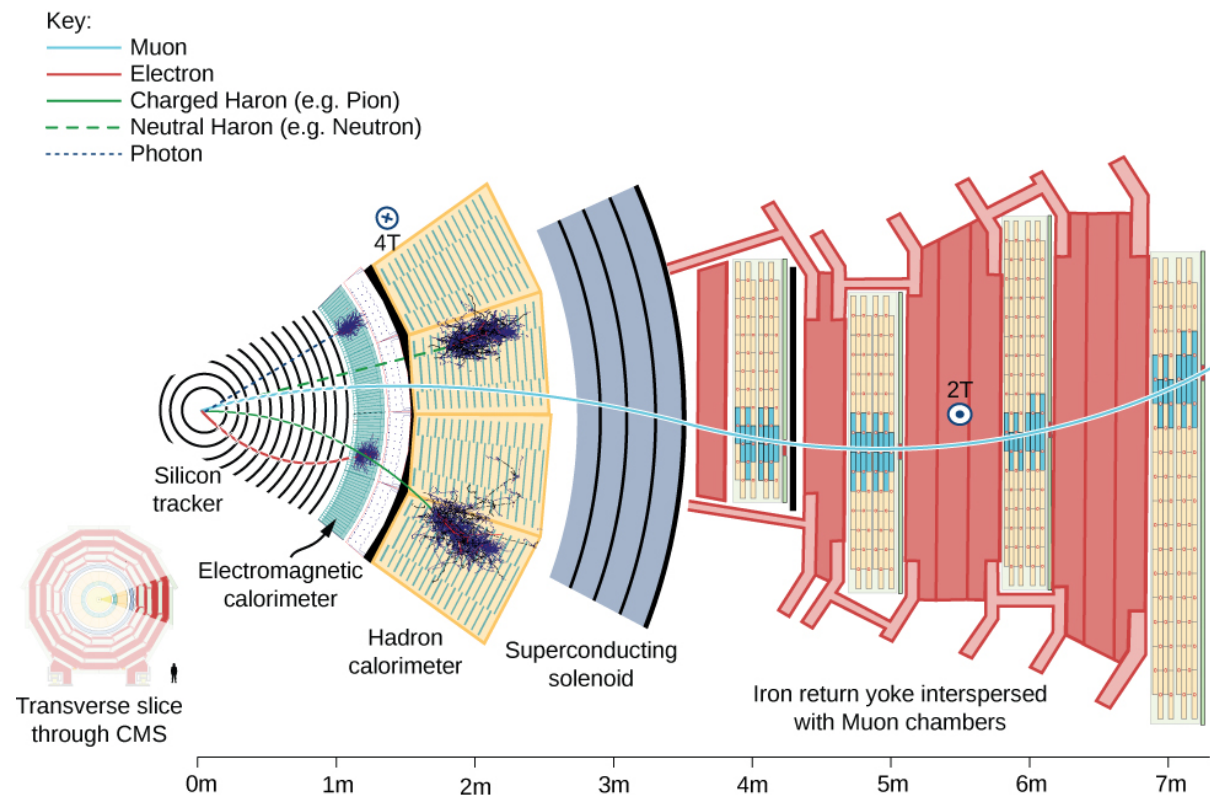


Figure 3.5: Percorso medio di una particella all'interno di CMS. Un muone, in azzurro, attraversa tutti i rivelatori percorrendo una traiettoria curva, lasciando segnale nel tracciatore, nei calorimetri e nelle varie stazioni per i muoni. Un elettrone, in rosso, lascia segnale nei tracciatori e viene assorbito dal calorimetro elettromagnetico. Un fotone, in azzurro tratteggiato, percorre una traiettoria dritta e sciamma soltanto nel calorimetro elettromagnetico, senza rilasciare segnale nel tracciatore. Un adrone, in verde (tratteggiato se neutro), lascia segnale nei tracciatori se carico e sciamma nel calorimetro adronico.

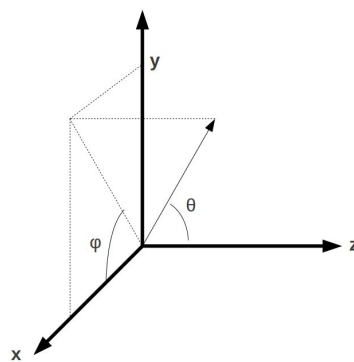


Figure 3.6: Coord sys.

⁵⁷⁵ che generano il campo scorre una corrente elettrica massima di 19 kA; l'energia massima
⁵⁷⁶ immagazzinata nel solenoide ammonta a 2.6 GJ.

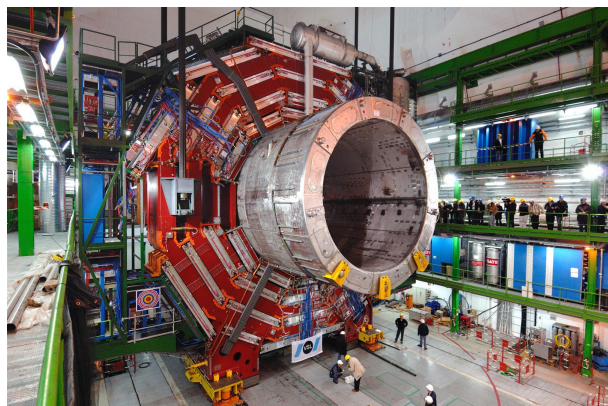


Figure 3.7: Solenoid.

⁵⁷⁷ **3.2.3 I tracciatori**

⁵⁷⁸ Il sistema dei tracciatori a CMS è interamente costituito da rivelatori al silicio. La loro elevata
⁵⁷⁹ precisione nella ricostruzione dei vertici secondari li rende strumenti di vitale importanza
⁵⁸⁰ per l'identificazione di quark (charm, beauty) e leptoni pesanti (τ), prodotti in numerosissimi
⁵⁸¹ processi fisici interessanti.

⁵⁸² I tracciatori coprono una pseudorapidità $|\eta| < 2.5$ per un'area attiva di circa 200 m^2 e sono
⁵⁸³ suddivisi nel pixel detector, più vicino al vertice di interazione, e nello strip detector, che
⁵⁸⁴ copre un raggio compreso tra 0.2 e 1.2 m. L'elevata granularità, come accennato, permette
⁵⁸⁵ di abbassare l'occupazione, vale a dire di avere meno eventi per ciascun sotto-rivelatore: i
⁵⁸⁶ pixel hanno un'area di $100 \times 150 \mu\text{m}^2$ e uno spessore di $285 \mu\text{m}$. Le strip adoperate a raggi
⁵⁸⁷ intermedi (20-55 cm) hanno dimensioni $10 \text{ cm} \times 80 \mu\text{m} \times 320 \mu\text{m}$; quelle a raggi maggiori
⁵⁸⁸ (55-110 cm) $25 \text{ cm} \times 180 \mu\text{m} \times 500 \mu\text{m}$. In totale ci sono 1440 moduli di pixel per un totale di
⁵⁸⁹ 66 milioni di canali di lettura, e 15148 moduli di strip per un totale di 9.3 milioni di canali di
⁵⁹⁰ lettura.

⁵⁹¹ L'altissima frequenza degli eventi implica l'utilizzo di un'elettronica capace di leggere molto
⁵⁹² rapidamente i segnali, portando ad un elevato consumo energetico: questo richiede un efficace
⁵⁹³ sistema di raffreddamento che mantenga il rivelatore ad una temperatura di $\approx 10^\circ \text{ C}$ in modo
⁵⁹⁴ da preservarne la durata.

⁵⁹⁵ Il pixel detector è costituito da tre strati di rivelatori nel barrel e da due dischi agli endcaps.
⁵⁹⁶ I moduli nel barrel sono disposti parallelamente al campo magnetico, mentre agli endcaps
⁵⁹⁷ sono inclinati di circa 20° : le coppie elettrone-lacuna prodotte nel semiconduttore sono allora
⁵⁹⁸ soggette ad una forza di Lorentz e il loro moto di deriva non avviene più lungo le linee del
⁵⁹⁹ campo elettrico, bensì esse si sparpagliano lungo diversi pixel. Calcolando il centro della
⁶⁰⁰ distribuzione di carica raccolta, è possibile determinare la posizione della particella carica che
⁶⁰¹ ha attraversato il rivelatore con una risoluzione di $15 \mu\text{m}$, sia nel piano $r\Phi$, sia lungo z .

⁶⁰² Il tracciatore a strip è composto da quattro sotto-sistemi: il tracker inner barrel, diviso in 4
⁶⁰³ strati; il tracker outer barrel, in 6 strati; il tracker inner disk, in 3 strati; il tracker endcaps, in 9
⁶⁰⁴ strati. I moduli più esterni, sia del barrel che dell'endcap, sono leggibili sia dal fronte che dal
⁶⁰⁵ retro.

⁶⁰⁶

3.2 CMS detector

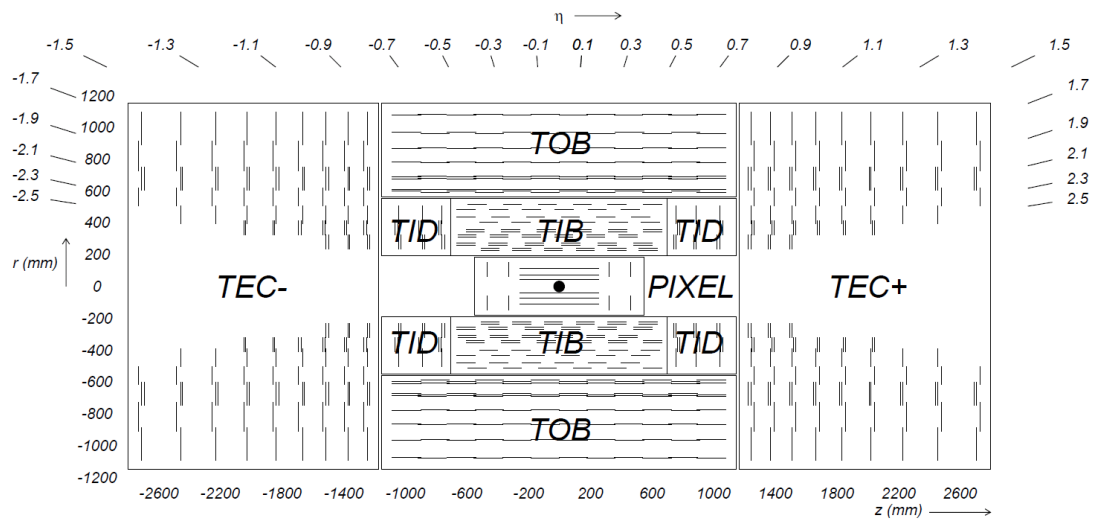


Figure 3.8: Tracker.

3.2.4 Il calorimetro elettromagnetico

Il calorimetro elettromagnetico di CMS è un rivelatore omogeneo composto da cristalli scintillatori di tungstenato di piombo (PbWO_4), ideali per le misure di fotoni ed elettroni. Il calorimetro è suddiviso in due gruppi di sotto-rivelatori, uno nel barrel ed uno per ciascun endcap; nel complesso copre una regione geometrica fino ad $|\eta| < 3$. Il PbWO_4 è stato scelto perché permette una risposta temporale rapida (in 25 ns, ad ogni collisione tra pacchetti, viene emesso l'85% della luce di scintillazione), ha elevate efficienze di scintillazione e resistenza alla radiazione. I 61200 cristalli impiegati nella regione di barrel hanno dimensioni $(22 \times 22) \text{ mm}^2 \times 23 \text{ cm}$, per una corrispondente lunghezza di radiazione di $25.8X_0$; i 7324 cristalli negli endcaps hanno dimensioni $28.6 \times 28.6 \text{ mm}^2 \times 22 \text{ cm}$, per una corrispondente lunghezza di radiazione di $24.7X_0$. Prima della regione di endcaps, è disposto un rivelatore di preshower costituito da due strati di sandwich piombo/silicio, per una lunghezza di radiazione di $3X_0$: questo permette una maggiore efficienza di rivelazione nella regione in avanti e permette di utilizzare cristalli più piccoli agli endcaps; è stato installato appositamente per distinguere due fotoni dal decadimento del π_0 e per poter indagare il canale di decadimento raro dell'Higgs $H \rightarrow \gamma\gamma$.

La luce scintillata nel barrel viene raccolta e amplificata da dei fotodiodi a valanga; agli endcaps, dove la frequenza degli eventi è più alta, il segnale è letto da fototridiodi a vuoto. La raccolta e l'amplificazione della radiazione da scintillazione è fortemente dipendente dalla temperatura, rendendo necessario un sistema di controllo e raffreddamento ad acqua che mantenga il calorimetro a 18° C costanti.

La risoluzione in energia del calorimetro è parametrizzata secondo l'espressione seguente:

$$\left(\frac{\sigma}{E}\right)^2 = \left(\frac{S}{\sqrt{E}}\right)^2 + \left(\frac{N}{E}\right)^2 + C^2, \quad (3.7)$$

dove S è il termine stocastico, N il contributo dal rumore, C un termine costante (contiene le dipendenze dalla calibrazione). In figura 3.10 sono mostrati i risultati ottenuti da misure di prova con un fascio di elettroni: le stime ottenute sono $S = 0.028 \text{ GeV}^{\frac{1}{2}}$, $N = 0.12 \text{ GeV}$, $C = 0.003$.

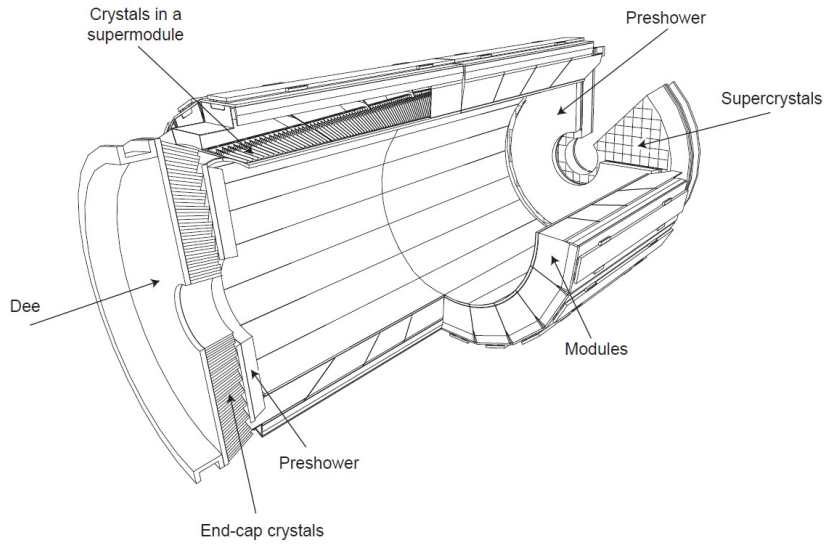


Figure 3.9: Ecal.

Figure 3.10: Risoluzione in energia di ECAL in funzione dell'energia del fascio di elettroni utilizzato per le misure. Sono mostrati anche i valori per i parametri di fit[16].

633 3.2.5 Il calorimetro adronico

- 634 Il calorimetro adronico è costruito a strati alterni di ottone e di scintillatore plastico. La qualità
 635 della misura dipende dalla granularità del rivelatore, dalla sua ermeticità e dalla frazione di
 636 energia depositata dagli adroni che il calorimetro è in grado di rivelare, quindi deve essere
 637 spesso abbastanza da assorbire tutti gli sciami adronici. L'estensione radiale del rivelatore
 638 nella regione di barrel è però limitata dalla presenza dell'ECAL e del solenoide supercondut-
 639 tore: per raggiungere una lunghezza di assorbimento sufficiente (11.8λ) è stato installato un
 640 ulteriore strato calorimetrico al di fuori del magnete.
 641 La luce di scintillazione, tipicamente nella parte blu-violetta dello spettro elettromagnetico,
 642 è interpretata da fibre ("wavelength shifter") che ne spostano la lunghezza d'onda al verde
 643 e la trasportano fino a fotorivelatori ibridi. I primi strati di scintillatore sono disposti im-
 644 mediamente a ridosso dell'ECAL, mentre gli ultimi a contatto con le camere per i muoni,
 645 permettendo così di raccogliere tutta l'informazione possibile.
 646 La risoluzione energetica combinata dei due calorimetri è data da:

$$\left(\frac{\sigma}{E}\right) \approx \frac{100\%}{\sqrt{E}} \oplus 45\%. \quad (3.8)$$

- 647 Le regioni di barrel e di endcaps dell'HCAL coprono un intervallo di $|\eta| < 3$; il calorimetro
 648 "forward" aggiuntivo arriva fino ad $|\eta| < 5.2$. Esso si trova a 11.2 m dal punto di interazione
 649 ed è stato progettato appositamente in previsione del raggiungimento dell'energia massima
 650 di 14 TeV: si calcola infatti che il deposito energetico medio di unadrone prodotto in collisioni
 651 pp in queste condizioni sia di 760 GeV nella direzione in avanti, da confrontare con i 100
 652 GeV medi delle altre regioni geometriche. Il calorimetro "forward" è composto da strati
 653 assorbitori di acciaio spessi 55 mm in cui sono innestate delle fibre di quarzo, che agisce da

3.2 CMS detector

mezzo attivo poiché rivela la luce Cherenkov emessa dalle particelle cariche dello sciamo, principalmente quella della componente elettromagnetica. La segmentazione longitudinale permette di distinguere i segnali lasciati dagli adroni rispetto a quelli lasciati da elettroni e fotoni.

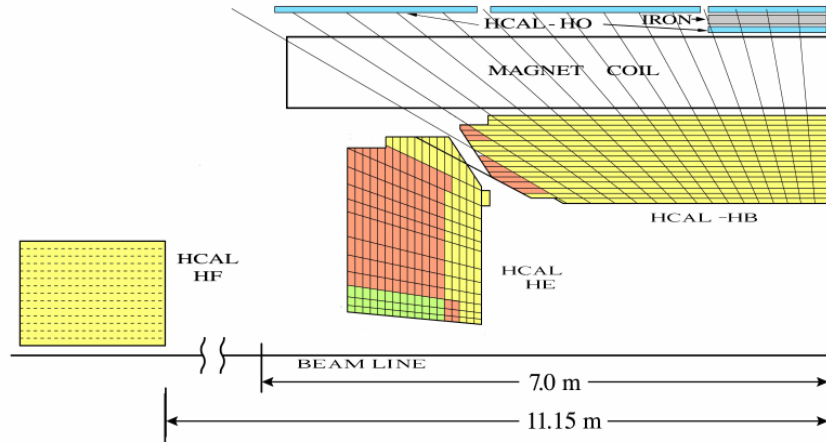


Figure 3.11: Hcal.

3.2.6 Sistema per l'identificazione dei muoni

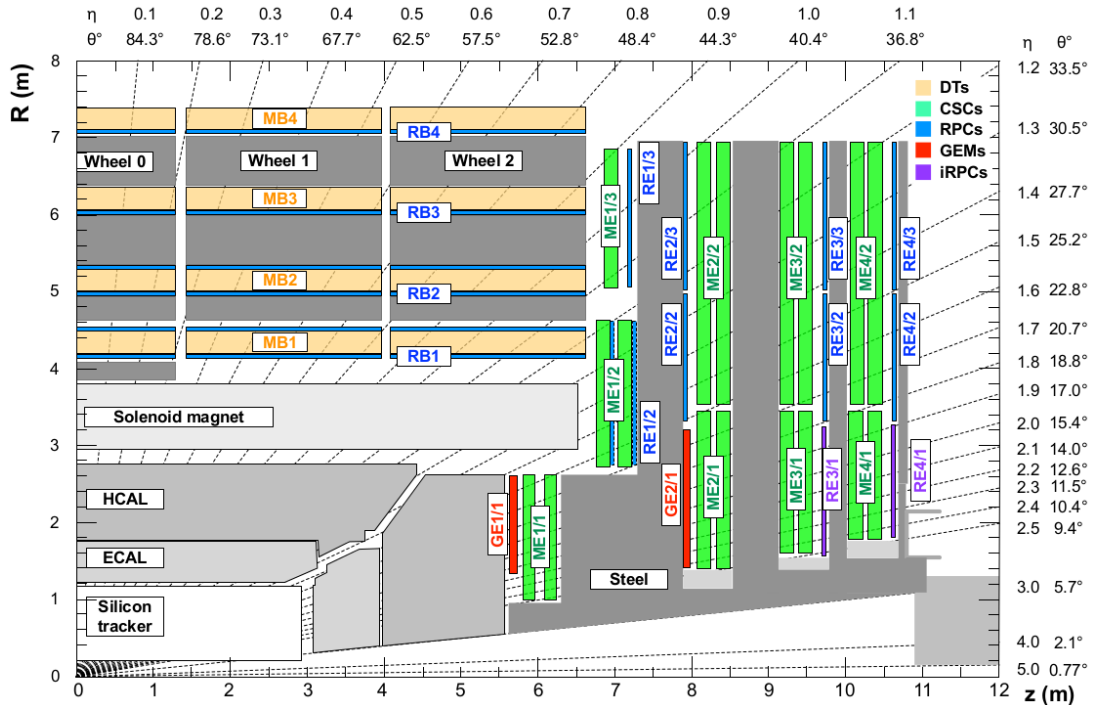


Figure 3.12: Mu.

L'ultimo gruppo di rivelatori di CMS consiste in una serie di rivelatori a gas per l'identificazione dei muoni, intervallati agli strati di ferro che chiudono le linee del campo magnetico

Figure 3.13: Sezione di CMS fatta parallelamente alla linea del fascio, nel piano rz. Si osservi in particolare la disposizione delle camere a muoni nel barrel (MB) e nell'endcap (ME).

661 generato dal solenoide. Nel barrel, le stazioni per i muoni sono separate in quattro cilindri
 662 concentrici; negli endcaps sono organizzate in tre dischi, ciascuno contenente quattro stazioni.
 663 Si può vedere la loro disposizione in figura 3.13.

664 Nella regione di barrel, dove ci sono meno muoni e meno neutroni di fondo e dove il campo
 665 magnetico è meno intenso, vengono utilizzate delle camere con tubi a deriva (DT, drift tube).
 666 Agli endcaps, dove i flussi sono maggiori, ci sono delle camere a strip catodici (CSC, cath-
 667 ode strip chambers), che permettono una risposta più rapida, una maggiore granularità e
 668 resistenza agli alti livelli di radiazione. Inoltre, dei rivelatori resistivi (RPC, resistive plate
 669 chamber) vengono sfruttati come ulteriore sistema di trigger indipendente per i muoni. In
 670 totale sono installati 250 DT, 540 CSC, 610 RPC.

- 671 • Ogni cella DT, di dimensioni di $42 \times 13 \text{ mm}^2$, contiene una miscela di gas (85% Ar e
 672 15% CO₂), un filo anodico a carica positiva e due strisce catodiche di alluminio (si veda
 673 la figura 3.2.6) che separano una cella dall'altra. Un piano di celle è isolato dall'altro
 674 mediante materiale plastico. L'anodo è realizzato da un filo di acciaio di 50 μm posto
 675 al centro della cella; in totale a CMS sono montati circa 195000 fili. La distanza della
 676 traccia dal filo è misurata dal tempo di deriva degli elettroni indotti dalla ionizzazione
 677 del gas: due strisce di elettrodi posizionate su due superfici della cella hanno l'obiettivo
 678 di dare forma al campo in modo da rendere la velocità di deriva quanto più uniforme
 679 possibile. La risoluzione spaziale complessiva del sistema è di 180 μm . Ogni camera con
 680 tubi a deriva (indicata con MB nella figura 3.13) ha una superficie di circa $2 \times 2.5 \text{ m}^2$ e
 681 contiene 12 strati di celle DT, arrangiate in tre gruppi di quattro. Il gruppo di celle di
 682 mezzo, i cui fili anodici sono disposti perpendicolarmente alla linea di fascio, misura la
 683 coordinata z, i due gruppi esterni, in cui i fili anodici sono paralleli al fascio, misurano
 684 la coordinata nel piano r Φ . Le camere di diverse stazioni sono sovrapposte in modo da
 685 coprire tutta la coordinata Φ .

- 686
 - 687 • Le CSC sono delle camere proporzionali a molti fili di forma trapezoidale. Sono costi-
 688 tuite da 6 piani con i fili anodici attraversati da 7 pannelli con strip catodiche di rame,
 689 tutto immerso in una miscela di gas. I fili anodici misurano la coordinata radiale r; le
 690 strisce catodiche sono disposte a Φ costante: interpolando la carica indotta nelle strip è
 691 possibile ricostruire anche la coordinata azimutale. Come nel caso dei DT, anche le CSC
 692 sono sovrapposte in modo da coprire tutta la coordinata Φ . A ciascun endcap ci sono 4
 693 stazioni di CSC che arrivano ad una regione geometrica di $|\eta| < 2.4$. Per $0.9 < |\eta| < 1.2$,
 694 un muone attraversa sia i DT del barrel che le CSC degli endcaps. Le CSC di CMS con-
 695 tengono, nel complesso, un volume di gas maggiore di 50 m^3 e più di 2 milioni di fili. Le
 696 CSC più grandi hanno dimensioni massime di 3.4 m lungo la direzione dei catodi e 1.5
 697 m lungo la direzione dei fili anodici. La risoluzione raggiungibile alla massima tensione
 698 è di circa 80 μm .

- 700 • Gli RPC sono dei piatti plastici ad alta resistività, separati da un volume riempito di gas,

701 e caricati a tensioni elevate, in modo da lavorare nel regime di ionizzazione a valanga.
702 I piatti sono provvisti di strisce di lettura che raccolgono il segnale al passaggio del
703 muone attraverso il gas. La loro risoluzione spaziale è molto bassa, circa 1-2 cm; al con-
704 trario la loro rapida risposta temporale (2-3 ns) e l'alta risoluzione (circa 1 ns) li rendono
705 strumenti ideali per il trigger e per la misura del tempo a cui avviene l'interazione. Nel
706 barrel sono montati 6 strati di RPC, negli endcaps ne sono montati 3.

707

708 L'intero sistema misura in maniera "standalone" l'impulso con una risoluzione in p_T di circa
709 $\Delta p_T / p_T \approx 8 - 15\%$ per muoni di $p_T = 10 \text{ GeV}/c$ e di $\Delta p_T / p_T \approx 20 - 40\%$ per muoni di $p_T = 1$
710 TeV/c . Combinando con la misura nei rivelatori al silicio la risoluzione passa rispettivamente
711 all'1% e al 7 – 16%.

712 Vista l'importanza dei muoni per il lavoro di tesi, nel prossimo capitolo illustrerò nel dettaglio
713 le tecniche utilizzate per la ricostruzione del segnale.

714 3.2.7 Altri rivelatori

715 Tracciatori e camere per i muoni coprono una regione di $|\eta| < 2.5$, gli apparati calorimetrici
716 arrivano fino ad $|\eta| < 5.2$. Ci sono altri due rivelatori che permettono misure nella regione
717 $5 \leq |\eta| \leq 11$, TOTEM e CASTOR. TOTEM sfrutta dei rivelatori a gas per le misure di scat-
718 tering elastico protone protone in funzione del loro momento. CASTOR è un calorimetro
719 elettromagnetico ed adronico che raccoglie luce Cherenkov, serve per misure di QCD in colli-
720 sioni p-p, p-ione, ione-ione.

721 3.2.8 Sistema di trigger

722 Il sistema di trigger di CMS è stato realizzato in funzione delle elevate luminosità e frequenza
723 di interazione; deve essere efficiente nello studio di fenomeni rari e molto diversi da loro, e
724 deve applicare delle selezioni in modo da abbassare la frequenza degli eventi da 40 MHz a
725 circa 100 Hz, tali da consentire la registrazione software. Esso deve inoltre avere tempi de-
726 cisionali molto brevi, dal momento che ogni 25 ns avviene una collisione: questo intervallo
727 temporale è troppo ristretto anche solo per poter leggere i dati raccolti dal rivelatore. Il pro-
728 blema viene superato operando le selezioni in fasi successive, in ciascuna delle quali vengono
729 prese delle decisioni sulla base di una sola parte dei dati. Il trigger di livello 1, L1, è un
730 dispositivo elettronico hardware che permette di scendere con la frequenza all'ordine di 100
731 kHz; il trigger di livello alto, HLT, è invece basato su algoritmi software capaci di rielaborare
732 il segnale, ed è a sua volta separato in due livelli logici (Level-2 e Level-3).

733

734 Il trigger di livello 1

735 Il trigger L1 ha accesso solamente alle informazioni provenienti dai calorimetri e dalle camere
736 per i muoni. Esso è segmentato in più processi in parallelo, ciascuno dei quali impiega sin-
737 golarmente meno di 25 ns. La decisione complessiva del L1 viene presa ogni $3.2 \mu\text{s}$, tenendo
738 conto anche dei tempi tecnici per il trasporto del segnale ai dispositivi: questo significa che la
739 parte puramente computazionale deve impiegare meno di 1 μs .

740 Il trigger di livello 1 è suddiviso in tre sistemi: il trigger calorimetrico, il trigger muonico, a
741 sua volta diviso in tre sotto-sistemi indipendenti per ciascuna categoria di rivelatori (DT, RPC,

742 CSC) e il trigger globale, che combina i risultati dei precedenti. Lo scopo del trigger muonico,
743 in particolare, è quello di identificare i muoni, ricostruirne la posizione e assegnarne delle
744 variabili relative al punto di collisione. Avere tre sottosistemi differenti permette di combi-
745 narne i rispettivi vantaggi: l'elevata risoluzione spaziale (dei DT e delle CSC) e l'eccellente
746 risoluzione temporale (degli RPC).

747 I trigger, più che operare delle vere e proprie decisioni autonome, hanno l'obiettivo di identi-
748 ficare dei precisi oggetti: elettroni/fotoni e muoni isolati o non isolati, jets centrali, in avanti o
749 provenienti da τ . I quattro candidati migliori di ciascuna categoria vengono mandati al trig-
750 ger globale insieme a: una misura della loro posizione, momento trasverso e ad un'etichetta
751 che ne identifica la qualità; informazioni di energia trasversa totale e mancante dal trigger
752 calorimetrico; un importante controllo sull'attività nella regione calorimetrica, che può essere
753 o meno compatibile con il deposito di energia lasciato dal passaggio di un muone. A questo
754 punto il trigger globale opera le selezioni necessarie, scegliendo uno o più oggetti che ab-
755 biano energia o momento sopra a una determinata soglia; si possono aggiungere richieste
756 sulla geometria, fino ad un massimo di 128 condizioni in parallelo. I trigger più semplici si
757 basano solitamente sulla presenza di un solo oggetto che abbia p_T o E_T sopra ad una certa
758 soglia (trigger "single-object"), oppure sulla presenza di due oggetti (trigger "di-object"), che
759 possono avere soglie identiche o differenti tra loro. In casi particolari, si può triggerare anche
760 su oggetti differenti.

761 Le scelte del trigger L1 devono sempre tenere conto della capacità del sistema di acquisizione
762 (Data Acquisition System), monitorato da un sistema di controllo del trigger. In alcuni casi, in
763 particolare per fenomeni con elevate sezioni d'urto (come ad esempio per le misure di fisica
764 del quark b), può essere utile ricorrere a trigger prescalati: gli eventi vengono scelti e salvati
765 a campione, in modo da garantire una sufficiente quantità di dati senza occupare eccessiva
766 memoria.

767

768 **L'High Level Trigger**

769 Se un evento è stato accettato dal trigger di livello 1, tutta l'informazione del rivelatore, che
770 ammonta a circa 1 MB, viene letta dal sistema di acquisizione ad una frequenza massima di
771 100 kHz e successivamente passata all'HLT. Gli algoritmi dell'HLT sono implementati nello
772 stesso software utilizzato per l'analisi offline e constano in una serie di passaggi che com-
773 prendono la ricostruzione del segnale e le selezioni. Ciascun oggetto processato con i criteri
774 voluti dall'HLT viene assegnato ad un preciso "trigger path" e successivamente salvato come
775 un sottocampione di eventi del campione filtrato dal L1.

776 **3.2.9 Il sistema di calcolo**

777 Il sistema di calcolo si occupa del salvataggio, del trasferimento e della manipolazione dei
778 dati raccolti da CMS; esso supporta inoltre la produzione e l'analisi di dati simulati ed infor-
779 mazioni sulla calibrazione degli apparati. Le risorse di calcolo non sono situate solo a CMS,
780 bensì sono distribuite in diversi centri detti "Tier", anche esterni al CERN, secondo una speci-
781 fica gerarchia. L'enorme mole di dati raccolti richiede grosse capacità computazionali ed un
782 metodo flessibile per ridurre le informazioni al minimo necessario senza ridondanze, ma che
783 permetta al contempo una grande varietà di operazioni ad ogni livello dell'analisi.
784 Il software di CMS, abbreviato in CMSSW, è sviluppato su un metodo di programmazione a

Figure 3.14: Rappresentazione dell'esperimento ATLAS.

oggetti, principalmente in linguaggio C++. L'unità base di ciascun tipo di dato, reale o simulato, è l'evento, Event: esso è un contenitore di molteplici informazioni, dal dato "grezzo" (RAW), al ricostruito (RECO), all'oggetto per l'analisi (AOD, Analysis Object Data) sul quale sono state applicate opportune selezioni. Tipicamente, i dati vengono rielaborati tramite moduli in linguaggio C++ o python; gli output vengono salvati in ROOT files.

790

791 3.3 ATLAS, ALICE, LHCb

792 3.3.1 ATLAS vs CMS

793 La ricerca di nuova fisica ad LHC viene portata avanti in collaborazione/competizione tra
794 due esperimenti simili tra loro, ATLAS e CMS. Prima di confrontare direttamente i limiti
795 ottenuti da entrambi, procedo a una breve descrizione dei due apparati e delle loro differenze.
796 Discuterò nel dettaglio l'esperimento CMS nel capitolo successivo.

797 ATLAS (A Toroidal LHC ApparatuS) e CMS (Compact Muon Solenoid) sono i due es-
798 perimenti di dimensioni maggiori dentro al tunnel di LHC, situati a 9 km di distanza tra
799 loro. Avere due rivelatori indipendenti capaci di osservare le medesime particelle è di vitale
800 importanza per un confronto incrociato in caso di scoperta.

801 ATLAS è un rivelatore cilindrico di 25 m di diametro e 46 m di lunghezza, dal peso di 7000
802 tonnellate. Il suo campo magnetico è prodotto all'interno da un solenoide, all'esterno da un
803 grande magnete toroidale (si veda la figura 3.14), capace di raggiungere i 2 T nel punto di
804 interazione.

805 Anche CMS è un cilindro, ma il suo campo magnetico di 3.8 T è interamente prodotto da un
806 grande solenoide centrale, le cui linee di campo sono chiuse da una rilevante quantità di ferro,
807 che serve anche da assorbitore per le particelle che lo attraversano.

808 Entrambi gli esperimenti sono strutturati in tre strati principali che avvolgono completamente
809 la linea di fascio attorno al punto di interazione. A ridosso dell'anello di accelerazione si
810 trovano gli array di rivelatori al silicio, necessari per precise misure posizionali delle tracce
811 cariche. Nel secondo strato, si trovano gli apparati calorimetrici: all'interno il calorimetro
812 elettromagnetico, per la misura dell'energia e posizione di elettroni e fotoni, all'esterno il
813 calorimetro adronico. La struttura più periferica serve per l'identificazione dei muoni. Gli
814 intensi campi magnetici permettono di misurare il momento e la carica delle particelle elettri-
815 camente cariche, che vengono deflesse per effetto della forza di Lorentz.

816 Viste le analogie strutturali e gli scopi comuni tra i due, elenco di seguito le differenze:

817 • *Tracciatori*: hanno una struttura sostanzialmente identica e presentano solo una dif-
818 ferenza nella risoluzione del momento trasverso p_T , migliore in CMS (principalmente
819 a causa del campo magnetico più intenso): $\sigma_{p_T}/p_T \approx 5 \cdot 10^{-4} p_T + 0.01$ per ATLAS;
820 $\sigma_{p_T}/p_T \approx 1.5 \cdot 10^{-4} p_T + 0.005$ per CMS.

821 • *Calorimetri elettromagnetici*: a CMS il calorimetro elettromagnetico è interamente con-
822 tenuto all'interno del solenoide, mentre in ATLAS è situato al suo esterno. Ciò com-
823 porta una perdita di energia delle particelle ed un conseguente peggioramento nella

risoluzione. Il calorimetro a cristalli di tungstenato di piombo di CMS ha una risoluzione sull'energia $\sigma_E/E \approx 3\%/\sqrt{E}$; quello a sandwich di argon liquido più assorbitori di piombo di ATLAS ha risoluzione $\sigma_E/E \approx 10\%/\sqrt{E}$.

- *Calorimetri adronici*: nel caso di CMS, soltanto una parte del calorimetro adronico è inclusa nel solenoide, ed essa non basta per assorbire completamente le particelle adroniche; si è perciò provveduto ad aggiungere un ulteriore strato calorimetrico al di fuori del magnete. Questa segmentazione abbassa il potere risolutivo. Il calorimetro a sandwich di ferro e scintillatore/rame ed argon liquido di ATLAS ha una risoluzione $\sigma_E/E \approx 50\%/\sqrt{E} + 0.03$ GeV; quello a ottone e scintillatore di CMS $\sigma_E/E \approx 100\%/\sqrt{E} + 0.05$ GeV.
- *Spettrometri per identificare i muoni*: in entrambi gli esperimenti, i rivelatori di muoni posti all'esterno del calorimetro, possono ricostruire la traccia del muone in maniera a sé stante ("standalone"). La particolare geometria per il sistema di magneti in ATLAS permette delle risoluzioni nettamente migliori nel momento in configurazione standalone, che resta attorno al 10% anche ad energie prossime ad 1 TeV. CMS invece risulta più preciso combinando le informazioni delle camere per i muoni con quelle dei tracciatori (7% ad 1 TeV rispetto al 35% per gli standalone).

3.3.2 Altri esperimenti

Per completezza, riassumo in breve gli scopi degli altri due esperimenti di LHC.

- ALICE (A Large Ion Collider Experiment) si occupa principalmente di studiare le collisioni tra nuclei pesanti (piombo) alle energie elevate disponibili ad LHC, con l'obiettivo di esplorare meglio la fisica adronica ad elevate densità, in condizioni in cui si forma una nuova fase detta quark-gluon plasma, di fondamentale interesse per comprendere a fondo la QCD.
- LHCb (Large Hadron Collider beauty) è un rivelatore per lo studio del quark b, in particolare per le violazioni di CP e per fenomeni rari associati agli adroni che lo contengono. L'obiettivo di queste ricerche è cercare una risposta per il problema dell'asimmetria materia-antimateria.

852

Chapter

4

Data and Monte Carlo samples

853

854

Physics objects

856

857

858 In this section, a list of the physics objects used in the analysis is presented, together with
 859 performance and validation plots.

860 The objects are selected according to the standard Run2 reccomendations provided by the
 861 various POGs for the Summer16 (25ns) MiniAOD-v2 (Moriond reccomendations).

862 The version of CMSSW used for the analysis is CMSSW_8_0_25.

863 **5.1 Vertex and Pile-up**

864 **How the vertices and pile-up are reconstructed**

865 Due to pileup several primary vertices are typically reconstructed in an event. The primary
 866 vertex of the event is defined as the one with the highest sum of transverse momenta $\sum p_T^2$ of
 867 clustered physics objects associated to it, which passes the following selections:

- 868 • number of degrees of freedom $N_{DoF} > 4$
- 869 • vertex position along the beampipe $|z_{vtx}| < 24\text{cm}$
- 870 • vertex distance with respect the beam pipe $d_0 < 2\text{cm}$

871 where z_{vtx} and d_0 are the distance along and perpendicular to the beam line of the vertex with
 872 respect the nominal interaction point $(0, 0, 0)$.

873 The data sample contains a significant number of additional interactions per bunch cross-
 874 ing, an effect known as pileup (PU).

875 The Summer16 v2 MINIAOD Monte Carlo samples are generated simulating the PU condi-
 876 tions, using the 25ns asymptotic PU scenario. Nevertheless, the MC PU description does not
 877 match exactly the conditions in data, and there is therefore the need to reweight the simulated
 878 events in order to improve the agreement with the data.

879 The MC samples are reweighted using the standard CMS PU reweighting technique [39,40]
 880 assuming a total inelastic cross section of $\sigma_{in} = 69\,200\,\mu\text{b}$.

881 The comparison between the distributions of primary vertices in data and MC after the PU
 882 reweighting is applied is shown in Figure 5.1 for an event selection (called inclusive selection)
 883 requiring large amount of E_T^{miss} recoiling against an AK8 fat jet (Tab. ??).

Figure 5.1: Primary vertices distributions after reweighting with the official recipe and $\sigma_{in} = 69\,200\mu b$.

884 5.2 Electrons

885 How the electrons are reconstructed

886 Electrons are reconstructed from energy deposits in the ECAL matched to tracks recon-
 887 structed in the silicon tracker. The electron trajectories are reconstructed using a dedicated
 888 modeling of the electron energy loss and fitted with a Gaussian sum filter. Electrons used in
 889 this analysis are required to pass the Particle Flow criteria, and to fall in the ECAL pseudora-
 890 pidity fiducial range ($|\eta| < 2.5$).

891 The electron identification used in this analysis is based on the “cut-based” Id defined
 892 by the EGamma POG for the Summer16 25ns [41], and suggested also for the usage in 80X
 893 for the so-called Moriond dataset. Isolation cuts are already applied within the cut-based
 894 Id definitions, therefore no additional Isolation cut is required. In the isolation definition
 895 the effect of PU is considered by taking into account the energy deposits in the calorimeter,
 896 estimated through the so-called ρ -area method, by subtracting the median energy density in
 897 the event ρ multiplied by electron effective area. The isolation value is computed in a ΔR cone
 898 of 0.3 centered along the lepton direction.

899 Since in this analysis we are aiming at a final state without any lepton, every electron
 900 identified with *veto* cut-based Id, transverse momentum $p_T > 10$ GeV is vetoed. The detailed
 901 set of cuts to define a *veto* cut-based Id electron are reported in the Table 5.1.

Electrons	Veto	
	EB	EE
$\sigma_{inj\eta}$	<	0.0115
$\Delta\eta_{in}^{seed}$	<	0.00749
$\Delta\varphi_{in}$	<	0.228
H/E	<	0.356
relIso (EA)	<	0.175
$ 1/E - 1/p $	<	0.299
$ d_0 $	<	0.05
$ d_z $	<	0.10
missing hits	\leq	2
conversion veto	yes	yes

Table 5.1: Summer16 cut-based selection for 25ns conditions. EB: barrel cuts ($|\eta_{supercluster}| \leq 1.479$); EE: endcap cuts ($|\eta_{supercluster}| > 1.479$)

902 Scale factors for electron identification (including isolation) are provided by Egamma POG,
 903 derived for 80X (Moriond 17 recommendation), that can be found in [42].

904 5.3 Muons

905 How the muons are reconstructed

5.3 Muons

906 In the standard CMS reconstruction for pp collisions, muon tracks are first reconstructed
907 independently in the inner tracker (tracker track) and in the muon system (standalone-muon
908 track). Based on these objects, two reconstruction approaches are used [43]: *Global Muon*
909 (*outside-in*) and *Tracker Muon* (*inside-out*).

910 *reconstruction (*outside-in*):* for each standalone-muon track, a matching tracker track is found by comparing pa-
911 rameters of the two tracks propagated onto a common surface, and a global-muon track
912 is fitted combining hits from the tracker track and standalone-muon track, using the
913 Kalman-filter technique [44]. At large transverse momenta, $p_T > 200\text{GeV}$, the global-
914 muon fit can improve the momentum resolution compared to the tracker-only fit.

915 *reconstruction (*inside-out*):* in this approach, all tracker tracks with $p_T > 0.5\text{GeV}$ and the total momentum $p >$
916 2.5GeV are considered as possible muon candidates and are extrapolated to the muon
917 system taking into account the magnetic field, the average expected energy losses, and
918 multiple scattering in the detector material. If at least one muon segment (i.e., a short
919 track stub made of DT or CSC hits) matches the extrapolated track, the corresponding
920 tracker track qualifies as a Tracker Muon.

921 Tracker Muon reconstruction is more efficient than the Global Muon reconstruction at low
922 momenta, $p_T \lesssim 5\text{GeV}$, because it requires only a single muon segment in the muon system,
923 whereas Global Muon reconstruction is designed to have high efficiency for muons penetrat-
924 ing through more than one muon station and typically requires segments in at least two muon
925 stations. Thanks to the high tracker-track efficiency and a very high efficiency of reconstruc-
926 tions in the muon system, about 99% of muons produced in pp collisions and having
927 sufficiently high momentum are reconstructed either as a Global Muon or a Tracker Muon,
928 and very often as both. Muons reconstructed only as standalone-muon tracks have worse
929 momentum resolution and less favorable collision muon to cosmic-ray muon ratio than the
930 Global and Tracker Muons and are usually not used in physics analyses.

931 Muons are usually based on the *Particle Flow Muon* selection, considering Global Muon or
932 a Tracker Muon candidates and by applying minimal requirements on the track components
933 in the muon system and taking into account a matching with small energy deposits in the
934 calorimeters.

935 For muons reconstructed using the PF algorithm, the standard muon isolation is defined as
936 the ratio of the p_T sum of all charged and neutral particle-flow candidates in the event within
937 a cone with a radius of $\Delta R = 0.4$ centered along the lepton direction. Corrections in order
to reduce the PU contamination are also applied, using the $\Delta\beta$ method. Charged candidates
falling into the cone that are not compatible with the primary vertex are removed from the
sum. Additionally, the neutral contribution from PU is estimated to be half the one coming
from charged candidates, and this quantity is also subtracted from the total. Eventually, the
scalar sum is divided by the lepton p_T itself. The general formula for the standard *particle-flow*
isolation is then:

$$I_{rel} = \left[\sum p_T^{\text{ch had}} + \max(\sum p_T^{\text{neu had}} + \sum p_T^\gamma - 0.5 \cdot \sum p_T^{\text{pu ch had}}, 0) \right] / p_T^\ell$$

938 where $\sum p_T^{\text{ch had}}$ is the sum of the transverse momenta of the charged hadrons, $\sum p_T^{\text{neu had}}$ is
939 the sum of transverse energies of the neutral hadrons, p_T^γ is the sum of the transverse energy
940 of particle flow photons and $\sum p_T^{\text{pu ch had}}$ is the sum of transverse momenta of the charged

938 particles in the cone of interest but with particles not originating from the primary vertex (for
 939 pileup corrections).

940 In the VZ event selection, all muons identified with the Loose standard id, p_T over 10 GeV,
 941 PF isolation below 0.25, $\eta < |2.4|$ are vetoed.

942 Scale factors for muon identification and isolation are centrally provided as a function of
 943 the muon p_T and η by the Muon POG [45], and are applied consistently in the analysis.

944 5.4 Taus

945 How the taus are reconstructed

946 The presence of hadronically-decaying taus only act as veto for the events both in the sig-
 947 nal and in the control regions to suppress electroweak backgrounds. The selection criteria
 948 for taus are $p_T > 18$ GeV and $|\eta| < 2.3$. The Run2 TauPOG recommended identification cri-
 949 teria [46] (`decayModeFinding`, `byLooseCombinedIsolationDeltaBetaCorr3Hits`) are required
 950 and applied in order to identify possible tau candidates.

951 5.5 Photons

952 How the photons are reconstructed

953 As in the case of tau leptons, a photon veto is applied in the analysis both for the signal
 954 and the control regions. Events are rejected if they contains one (or more) photon with $p_T > 15$
 955 GeV, $|\eta| < 2.5$, passing the Loose cut-based photon ID. The Loose photon Id is applied as
 956 in the EGamma POG recommandations for Run2 analyses [47] (tuned on Spring16 25 ns
 957 samples). The isolation cuts (using the rho-area method for the mitigation of the pileup) and
 958 conversion safe electron veto are applied. The isolation value is computed in a ΔR cone of
 959 0.3 and is corrected for pileup by subtracting the event-by-event energy density (ρ) times an
 960 effective area. The applied cut-based definition of the Loose photon Id is reported in Table 5.2.

Photons	Loose	
	EB	EE
H/E	<	0.0597
$\sigma_{i\eta i\eta}$	<	0.01031
PF ch.had.iso.(ρ -corr)	<	1.295
PF neu.had.iso.(ρ -corr)	<	$10.910 + 0.0148p_T + 0.000017p_T^2$
PF photon iso.(ρ -corr)	<	$5.931 + 0.0163p_T + 0.000014p_T^2$
conversion veto	yes	6.641 + 0.0034 p_T

Table 5.2: Photon cut-based Id for Spring16 25ns conditions. EB: barrel cuts ($|\eta_{\text{supercluster}}| \leq 1.479$); EE: endcap cuts ($|\eta_{\text{supercluster}}| > 1.479$)

961

962 Scale factors for photon identification (including isolation) are provided by Egamma POG,
 963 derived for 80X (Moriond 17 recommendation), that can be found in [42].

5.6 Jets

How the jets are reconstructed

Events in the CMS detector are reconstructed using the particle-flow algorithm [48, 49], which combines information from all sub-detectors in order to reconstruct stable particles (muons, electrons, photons, neutral and charged hadrons). The charged hadron subtraction algorithm (CHS) removes candidates not associated to the primary vertex in order to remove contributions from pileup [50]. The remaining particles are used as input to jet clustering algorithms to reconstruct particle-flow jets. The jets are clustered using the FASTJET package [?] with the anti- k_T jet clustering algorithm [51] with a clustering parameter of $R = 0.8$ (“fat”-jets or AK8 jets) or $R = 0.4$ (“standard”-jets or AK4 jets). In order to avoid double-counting of PF candidates, AK4 jets are considered only if the angular separation from the leading AK8 jet is larger than $\Delta R > 0.8$. Several levels of jet energy corrections are applied to the momentum of the clustered (raw) jets in order to obtain the energy value that is closer to the true energy of the initial parton [52]:

L1 Offset: the pileup and electronic noise effects are removed. This correction can be estimated using events collected by a random trigger, without any preconditions except a beam crossing, referred as *zero bias* events. The offset contribution from pileup is estimated by the FastJet method which relies on the definition of a jet area [?] from which a median energy density (ρ , in GeV/Area) per event can be defined. The correction subtracted to the jet p_T equals to ρ times the jet area. FastJet has the advantage of being able to remove the out-of-time pileup component, but has the disadvantage of subtracting the underlying event contribution as well.

L2 Relative (η): the variation in jet response with η is flattened. The unbalance between the jets transverse momentum that is observed on average, is due to the variation of the jet response across the detector versus η .

L3 Absolute (p_T): the calorimetric energy response varies as a function of the jet p_T . The absolute correction removes these variations and makes the response equal to unity. This correction is obtained from simulation using the Monte Carlo truth information.

L2L3 Residual: differences between data and simulation after L2 and L3 corrections are removed by applying a specific calibration to data events. Residual corrections are extracted from data using the transverse momentum balance in γ +jets and Z +jets events [52].

The latest jet energy corrections are applied to AK4 and AK8 CHS jets, and the tags are Summer16 23Sep2016V3.

In this analysis, jets are considered if the corrected p_T is larger than 30 GeV for AK4 jets and 200GeV for AK8 jets, and lie in the tracker acceptance ($|\eta| < 2.4$). Additionally, AK4 are required to pass *loose* jet identification requirements, AK8 are required to pass *tight* jet identification requirements defined by the JETMET POG for Run2 analyses [53], listed in Table 5.3. AK8 jets are used to reconstruct the hadronically decaying electroweak boson candidate, whilst AK4 jets are used to suppress the contribution of top and QCD background events.

Figure 5.2- 5.4 show the data/simulation comparison after the analysis selections (Tab. ?? without Top cleaning and Event cleaning).

PF Jet ID	<i>loose</i>	<i>tight</i>
Neutral Hadron Fraction	< 0.99	< 0.90
Neutral EM Fraction	< 0.99	< 0.90
Number of Constituents	> 1	> 1
Muon Fraction	-	-
Additionally, for $ \eta < 2.4$		
Charged Hadron Fraction	> 0	> 0
Charged Multiplicity	> 0	> 0
Charged EM Fraction	< 0.99	< 0.99

Table 5.3: *Loose* and *Tight* jet identification requirements for Run2 (Spring16) 25ns conditions.

Figure 5.2: Number of reconstructed AK8 jets after selections.

Figure 5.3: Leading AK8 jet p_T spectra after selections.

Figure 5.4: Leading AK8 jet η spectra after selections.

1006 Since it has been measured that the jet energy resolution (JER) is not the same in data and
 1007 MC, an additional smearing is applied in simulation, in order to get a better agreement, as
 1008 suggested by JETMET POG [54].

There are two independent ways to get the smearing. With the scaling method, corrected four-momentum of a reconstructed jet is rescaled with a factor

$$c_{\text{JER}} = 1 + (s_{\text{JER}} - 1) \frac{p_T - p_T^{\text{ptcl}}}{p_T},$$

where p_T is its transverse momentum, p_T^{ptcl} is the transverse momentum of the corresponding jet clustered from generator-level particles, and s_{JER} is the data-to-simulation core resolution scale factor. Factor c_{JER} is truncated at zero, i.e. if it is negative, it is set to zero. This method only works if a well-matched particle-level jet is present and can result in a large shift of the response otherwise. The following requirements are imposed for the matching:

$$\Delta R < R_{\text{cone}}/2, |p_T - p_T^{\text{ptcl}}| < 3\sigma_{\text{JER}} p_T.$$

1009 Here R_{cone} is the jet cone size parameter (for instance, 0.4 for AK4 jets) and σ_{JER} is the relative
 1010 p_T resolution as measured in simulation.

An alternative approach, which does not require the presence of a matching particle-level jet, is the stochastic smearing. In this case corrected jet four-momentum is rescaled with a factor

$$c_{\text{JER}} = 1 + \mathcal{N}(0, \sigma_{\text{JER}}) \sqrt{\max(s_{\text{JER}}^2 - 1, 0)},$$

1011 where σ_{JER} and s_{JER} are the relative p_T resolution in simulation and data-to-simulation scale
 1012 factors, and $\mathcal{N}(0, \sigma)$ denotes a random number sampled from a normal distribution with a

5.6 Jets

1013 zero mean and variance σ^2 . As before, scaling factor c_{JER} is truncated at zero. This method
1014 only allows to degrade the resolution.

1015 The smearing procedure adopted in this analysis is the hybrid method: when matching
1016 particle-level jet is found, the scaling method is used; otherwise the stochastic smearing is
1017 applied. The smearing coefficients and their errors, provided by JETMET POG, are reported
1018 in Tab. 5.4 for 2016 data (tag: Spring1625nsV10).

Jet η	SF
0.0 – 0.5	1.109 ± 0.008
0.5 – 0.8	1.138 ± 0.013
0.8 – 1.1	1.114 ± 0.013
1.1 – 1.3	1.123 ± 0.024
1.3 – 1.7	1.084 ± 0.011
1.7 – 1.9	1.084 ± 0.011
1.9 – 2.1	1.140 ± 0.047
2.1 – 2.3	1.067 ± 0.053
2.3 – 2.5	1.177 ± 0.041
2.5 – 2.8	1.364 ± 0.039
2.8 – 3.0	1.857 ± 0.071
3.0 – 3.2	1.328 ± 0.022
3.2 – 5.0	1.16 ± 0.029

Table 5.4: Smearing coefficients and JER uncertainties.

1019 **5.6.1 Jet mass**

1020 The jet mass is the main observable in distinguishing a V-jet from a QCD jet. Jet grooming
 1021 consists in the suppression of uncorrelated UE/PU (underlying event and pile-up) radiation
 1022 from the target jet and improves the discrimination pushing the jet mass for QCD jets towards
 1023 lower values while maintaining the jet mass for V-jets around the boson-mass.

1024 The grooming algorithm considered in this analysis is the following:

Soft-drop: The “soft drop declustering” is a jet substructure technique which recursively removes soft wide-angle radiation from a jet [55]. The soft drop algorithm depends on two parameters: a soft threshold z_{cut} and an angular exponent β . Like any grooming method, soft drop declustering removes wide-angle soft radiation from a jet in order to mitigate the effects of contamination from initial state radiation (ISR), underlying event (UE), and multiple hadron scattering (pileup). Given a jet of radius R_0 with only two constituents, the soft drop procedure removes the softer constituent unless:

$$\frac{\min(p_T^1, p_T^2)}{p_T^1 + p_T^2} > z_{cut} \left(\frac{\Delta R_{12}}{R_0} \right)^\beta$$

1025 By construction, this condition fail for wide-angle soft radiation. The degree of jet
 1026 grooming is controlled by z_{cut} and β , with $\beta \rightarrow \infty$ returning back an ungroomed jet.
 1027 The $\beta = 0$ limit of the energy loss is particularly interesting, since it is largely insensitive
 1028 to the value of the strong coupling constant. The default parameters used by CMS are
 1029 $\beta = 0$ and $z_{cut} = 0.1$.

1030 The grooming algorithm, **soft-drop**, is used in association with **PUPPI** in order to remove
 1031 soft and wide-angle radiations and the pile-up contribution. It is a shared choice among all
 1032 the diboson analyses, praised by theoreticians.

1033 Unfortunately, the default soft-drop + PUPPI jet mass suffers from a systematic shift from
 1034 the expected value of about $\sim 10\%$, and some residual dependence on the jet p_T . Further
 1035 corrections to the jet mass have been applied:

1036 **Gen:** a p_T -dependent correction to account for a small shift in the generated vector boson
 1037 mass, applied only on simulated samples

1038 **Reco:** a p_T -dependent correction to the reconstructed jet mass, applied separately for jets in
 1039 the barrel and endcaps regions

1040 These corrections are evaluated centrally by JMAR and documented in [56], and applied
 1041 accordingly within the analysis.

1042 Figure 5.6- 5.7 show the jet mass for W or Z bosons before and after the correction, without
 1043 applying any cut on this variable.

Figure 5.5: Softdrop + PUPPI mass of AK8 jet reconstructed for different bulk graviton signal samples; left: before corrections. right: after corrections.

1044 Furthermore, in order to obtain a better data-Monte Carlo agreement, a smearing proce-
 1045 dure has been applied to the puppi softdrop mass, by using the stochastic method, with a
 1046 constant smearing coefficient provided by JETMET POG (1.00 ± 0.20), that does not depend on
 1047 jet pseudorapidity if it is restricted to $|\eta| < 2.5$.

Figure 5.6: Softdrop + PUPPI mass of AK8 jet reconstructed for different W' signal samples; left: before corrections. right: after corrections.

Figure 5.7: Softdrop + PUPPI mass of AK8 jet; left: before corrections. right: after corrections.

1048 **5.6.2 Jet substructure**

In order to further discriminate signal from background, it is useful to investigate the inner structure of the jet. Studying the distribution of the jet constituents with respect to the jet axis allows us to test the hypothesis of the existence of multiple substructures, that could be evidence of jets originated by more than one parton. This procedure proceeds as follows: the constituents of the jet are clustered again with the k_T algorithm, however the procedure is stopped when one obtains N subjets. Then, a new variable, the N-subjettiness, is introduced. It is defined as:

$$\tau_N = \frac{1}{d_0} \sum_k p_{T,k} \min(\Delta R_{1,k}^\beta, \Delta R_{2,k}^\beta, \dots, \Delta R_{N,k}^\beta)$$

1049 where β is an arbitrary parameter, the index k runs over the jet constituents and the distances
1050 $\Delta R_{N,k}$ are calculated with respect to the axis of the N-th subjet, obtained by one iteration of τ
1051 minimization by varying the subjet axes around the k_T subjet axes.

The normalization factor d_0 is calculated as $d_0 = \sum_k p_{T,k} R_0^\beta$, setting R_0 to the radius of the original jet. The N-subjettiness is always included in the interval from 0 to 1 and represents the compatibility of the jet structure with an N-subjet hypothesis: small values correspond to high compatibility. Indeed, τ_N weights the transverse momentum of the jet constituents by their angular distance to the closest subjet. In this analysis the N-subjettiness is calculated from the ungroomed jet with the parameter $\beta = 1$. The subjettiness related to the one and two subjet hypothesis is thus:

$$\tau_1 = \frac{1}{d_0} \sum_k p_{T,k} \Delta R_{1,k}$$

and

$$\tau_2 = \frac{1}{d_0} \sum_k p_{T,k} \min(\Delta R_{1,k}, \Delta R_{2,k})$$

1052 In principle, these two quantities should allow us to distinguish the dipole-like nature of the
1053 showering of the Higgs decay from the classic monopole structure of QCD jets. In particular,
1054 the variable that best discriminates between V-jets and QCD jets is the ratio of 2-subjettiness
1055 and 1-subjettiness, $\tau_{21} = \tau_2 / \tau_1$.

1056 Figure 5.8 shows the τ_{21} distributions for the PUPPI algorithm.

Figure 5.8: τ_{21} subjettiness of PUPPI AK8 jet after inclusive selections.

1057 5.7 b-tagging

1058 B-tagging algorithms are applied to both the fat-jet and the sub-jets, independently. For sub-
 1059 jets, run-II taggers are by default applied on the same charged particle-flow candidate list that
 1060 is used in the jet clustering (*explicit jet-to-track association*). Thanks to the explicit jet-to-track
 1061 association, the two sub-jets do not share any PF-constituent, avoiding unintended correla-
 1062 tions.

1063 The jet or sub-jet is considered as tagged if the discriminator value is above some threshold
 1064 value, often referred to as the cut value, and the efficiency is defined as the number of jets
 1065 which have a discriminator value that is above that cut divided by the total number of jets (of
 1066 the same flavor).

1067 The b-tagging algorithm used to set the analysis strategy is the Combined Secondary Ver-
 1068 tex (CSV) [57] discriminator (full name `pfCombinedInclusiveSecondaryVertexV2BJetTags`).
 1069 Different working points are provided by the POG for Run2 analyses [58], as shown in ta-
 1070 ble 5.7, but the only one used in this analysis is the *loose* working point.

Working point	CSV cut	mis-tag probability
CSVL (Loose)	> 0.5426	$\approx 10\%$
CSVM (Medium)	> 0.8484	$\approx 1\%$
CSVT (Tight)	> 0.9535	$\approx 0.1\%$

Table 5.5: Working point for CSV b-tagging algorithm.

1071 B-tagging efficiency is not the same in data and MC. In order to take into account this dif-
 1072 ference, the BTV POG provides collections of b-tagging scale factors for b-jets and mistagged
 1073 light jets, measured for different physics processes, for the supported tagging algorithms and
 1074 the three standard working points [57]. A weight is calculated on a per-event basis as a func-
 1075 tion of the b-tagging status of the jets and their kinematic variables [59].

1076 In this analysis, b-tagging is used in order to reject events where a top quark is involved,
 1077 by asking to the AK4 jets not laying in the AK8 jet cone to be anti b-tagged (in practice, the
 1078 maximum CSV value allowed is the loose working point, CSVL).

1079 5.8 Missing Energy

1080 How the MET is reconstructed

1081 The E_T^{miss} is the imbalance in the transverse momentum of all visible particles, and it is
 1082 reconstructed with the particle flow algorithm [48]. The *raw* E_T^{miss} is defined as the inverse vec-
 1083 torial sum of the transverse momentum of all the reconstructed charged and neutral particle
 1084 flow candidates: $E_T^{\text{miss}} = -\sum_{i=0}^{\text{all}} \vec{p}_{T,i}$. The raw E_T^{miss} is systematically different from true E_T^{miss} ,
 1085 for many reasons including the non-compensating nature of the calorimeters and detector
 1086 misalignment. To better estimate the true E_T^{miss} , corrections can be applied:

1087 *Type-0*: a mitigation for the degradation of the E_T^{miss} reconstruction due to the pileup interac-
 1088 tions, by applying the CHS algorithm. However, the E_T^{miss} contribution from pileup
 1089 neutral particles cannot be easily subtracted; the assumption is that the E_T^{miss} contribu-
 1090 tion term of charged and neutral pileup particles are the same, and cancellation at the
 1091 true level is exact: $\sum_{\text{neuPU}} \vec{p}_{T,i}^{\text{true}} + \sum_{\text{chPU}} \vec{p}_{T,i}^{\text{true}} = 0$. An additional E_T^{miss} term is then

5.8 Missing Energy

added to the raw E_T^{miss} to take into account the neutral PU contribution, which is equal to the charged one with a multiplicative scale factor taking into account calorimeter mismeasurements of low- p_T energy deposits.

Type-1: propagation of the jet energy corrections (JEC) to MET. The Type-I correction replaces the vector sum of transverse momenta of particles which can be clustered as jets with the vector sum of the transverse momenta of the jets to which JEC is applied.

Particle flow E_T^{miss} with type-1 corrections applied is currently the default one used by CMS physics analyses. Additionally, some E_T^{miss} filters have been recommended by JETMET POG for Run2 analyses [53], in order to remove events with spurious E_T^{miss} related to detector noise and bad reconstructions, and they are listed in sec. ??.

Since the E_T^{miss} corrections and uncertainties depend on the JEC applied, they are re-computed accordingly following the JETMETPOG recommendation:

```
from PhysicsTools.PatUtils.tools.runMETCorrectionsAndUncertainties import
runMetCorAndUncFromMiniAOD
# If you only want to re-correct and get the proper uncertainties
runMetCorAndUncFromMiniAOD(process,
                             isData=True (or False),
                             )
process.p = cms.Path(process.fullPatMetSequence *
                     process.yourAnalyzer)
cms.InputTag("slimmedMETs", "", "YourProcessName")
```

Figure 5.9 show the E_T^{miss} distribution for data and Monte Carlo after the corrections and filters.

Figure 5.9: Type-1 corrected E_T^{miss} distribution after inclusive selections.

1116

Chapter

6

Diboson candidate reconstruction

1117

1118

1119

Chapter

7

Background estimation

1120

1121

1122

Chapter

8

Systematic uncertainties

1123

1124

1125

Chapter

9

Results

1126

1127

1128

Chapter

10

Conclusions

1129

1130

1131

Bibliography

1132

1133

- 1134 [1] G. Aad *et al.*, "Observation of a new particle in the search for the Standard Model Higgs
1135 boson with the ATLAS detector at the LHC," *Phys. Lett. B*, vol. 716, p. 1, 2012.
- 1136 [2] S. Chatrchyan *et al.*, "Observation of a new boson at a mass of 125 GeV with the CMS
1137 experiment at the LHC," *Phys. Lett. B*, vol. 716, p. 30, 2012.
- 1138 [3] S. Chatrchyan *et al.*, "Observation of a new boson with mass near 125 GeV in pp collisions
1139 at $\sqrt{s} = 7$ and 8 TeV," *JHEP*, vol. 06, p. 081, 2013.
- 1140 [4] G. Aad *et al.*, "Evidence for the spin-0 nature of the Higgs boson using ATLAS data,"
1141 *Phys. Lett. B*, vol. 726, p. 120, 2013.
- 1142 [5] V. Khachatryan *et al.*, "Precise determination of the mass of the Higgs boson and tests of
1143 compatibility of its couplings with the standard model predictions using proton collisions
1144 at 7 and 8 TeV," *Eur. Phys. J. C*, vol. 75, p. 212, 2015.
- 1145 [6] G. Aad *et al.*, "Measurement of the Higgs boson mass from the $H \rightarrow \gamma\gamma$ and $H \rightarrow ZZ^* \rightarrow$
1146 4ℓ channels in pp collisions at center-of-mass energies of 7 and 8 TeV with the ATLAS
1147 detector," *Phys. Rev. D*, vol. 90, p. 052004, 2014.
- 1148 [7] CMS and ATLAS Collaborations, "Combined Measurement of the Higgs Boson Mass in
1149 pp Collisions at $\sqrt{s} = 7$ and 8 TeV with the ATLAS and CMS Experiments." Submitted
1150 to *Phys. Rev. Lett.*, 2015.
- 1151 [8] G. Degrassi, S. Di Vita, J. Elias-Miro, J. R. Espinosa, G. F. Giudice, G. Isidori, and A. Stru-
1152 mua, "Higgs mass and vacuum stability in the Standard Model at NNLO," *JHEP*, vol. 08,
1153 p. 098, 2012.
- 1154 [9] D. Pappadopulo, A. Thamm, R. Torre, and A. Wulzer, "Heavy vector triplets: bridging
1155 theory and data," *Journal of High Energy Physics*, vol. 2014, no. 9, pp. 1–50, 2014.
- 1156 [10] V. D. Barger, W.-Y. Keung, and E. Ma, "A Gauge Model With Light W and Z Bosons,"
1157 *Phys. Rev.*, vol. D22, p. 727, 1980.

- 1158 [11] C. Grojean, E. Salvioni, and R. Torre, "A weakly constrained W' at the early LHC," *JHEP*,
1159 vol. 07, p. 002, 2011.
- 1160 [12] R. Contino, D. Pappadopulo, D. Marzocca, and R. Rattazzi, "On the effect of resonances
1161 in composite higgs phenomenology," *Journal of High Energy Physics*, vol. 2011, no. 10,
1162 pp. 1–50, 2011.
- 1163 [13] B. Bellazzini, C. Csáki, and J. Serra, "Composite Higgses," *Eur. Phys. J.*, vol. C74, no. 5,
1164 p. 2766, 2014.
- 1165 [14] G. F. Giudice, C. Grojean, A. Pomarol, and R. Rattazzi, "The Strongly-Interacting Light
1166 Higgs," *JHEP*, vol. 06, p. 045, 2007.
- 1167 [15] A. Wulzer, "An Equivalent Gauge and the Equivalence Theorem," *Nucl. Phys.*, vol. B885,
1168 pp. 97–126, 2014.
- 1169 [16] A. M. Sirunyan *et al.*, "Search for massive resonances decaying into WW, WZ, ZZ, qW,
1170 and qZ with dijet final states at $\sqrt{s} = 13$ TeV," 2017.
- 1171 [17] CMS Collaboration, "Search for massive resonances decaying into WW, WZ, ZZ, qW and
1172 qZ in the dijet final state at $\sqrt{s} = 13$ TeV," CMS Physics Analysis Summary CMS-PAS-
1173 B2G-17-001, CERN, Geneva, 2017.
- 1174 [18] C. Collaboration, "Search for heavy resonances decaying into a vector boson and a Higgs
1175 boson in hadronic final states with 2016 data," 2017.
- 1176 [19] CMS Collaboration, "Search for heavy resonances decaying into a vector boson and a
1177 Higgs boson in hadronic final states with 2016 data," CMS Physics Analysis Summary
1178 CMS-PAS-B2G-17-002, CERN, Geneva, 2017.
- 1179 [20] CMS Collaboration, "Search for heavy resonances decaying into a Z boson and a W
1180 boson in the $\ell^+ \ell^- q\bar{q}$ final state," CMS Physics Analysis Summary CMS-PAS-B2G-16-022,
1181 CERN, Geneva, 2017.
- 1182 [21] V. Khachatryan *et al.*, "Search for heavy resonances decaying into a vector boson and a
1183 Higgs boson in final states with charged leptons, neutrinos, and b quarks," *Phys. Lett.*,
1184 vol. B768, pp. 137–162, 2017.
- 1185 [22] CMS Collaboration, "Search for new resonances decaying to $WW/WZ \rightarrow \ell\nu qq$," CMS
1186 Physics Analysis Summary CMS-PAS-B2G-16-020, CERN, Geneva, 2016.
- 1187 [23] CMS Collaboration, "Search for heavy resonances decaying into a Z boson and a vector
1188 boson in the $\nu\nu q\bar{q}$ final state," CMS Physics Analysis Summary CMS-PAS-B2G-17-005,
1189 CERN, Geneva, 2017.
- 1190 [24] M. Aaboud *et al.*, "Search for diboson resonances with boson-tagged jets in pp collisions
1191 at $\sqrt{s} = 13$ TeV with the ATLAS detector," 2017.
- 1192 [25] ATLAS Collaboration, "Search for WW/WZ resonance production in $\ell\nu qq$ final states in
1193 pp collisions at $\sqrt{s} = 13$ TeV with the ATLAS detector," ATLAS Conference Note ATLAS-
1194 CONF-2017-051, CERN, Geneva, Jul 2017.

BIBLIOGRAPHY

- 1195 [26] “Searches for heavy ZZ and ZW resonances in the llqq and vvqq final states in pp col-
1196 lisions at $\text{sqrt}(s) = 13 \text{ TeV}$ with the ATLAS detector,” ATLAS Conference Note ATLAS-
1197 CONF-2016-082, CERN, Geneva, Aug 2016.
- 1198 [27] M. Aaboud *et al.*, “Search for heavy resonances decaying to a W or Z boson and a Higgs
1199 boson in the $q\bar{q}^{(\prime)} b\bar{b}$ final state in pp collisions at $\sqrt{s} = 13 \text{ TeV}$ with the ATLAS detector,”
1200 2017.
- 1201 [28] ATLAS Collaboration, “Search for heavy resonances decaying to a W or Z boson and a Higgs
1202 boson in final states with leptons and b -jets in 36.1 fb^{-1} of pp collision data at
1203 $\sqrt{s} = 13 \text{ TeV}$ with the ATLAS detector,” ATLAS Conference Note ATLAS-CONF-2017-
1204 055, CERN, Geneva, Jul 2017.
- 1205 [29] L. Randall and R. Sundrum, “A Large mass hierarchy from a small extra dimension,”
1206 *Phys. Rev. Lett.*, vol. 83, pp. 3370–3373, 1999.
- 1207 [30] L. Randall and R. Sundrum, “An Alternative to compactification,” *Phys. Rev. Lett.*, vol. 83,
1208 pp. 4690–4693, 1999.
- 1209 [31] K. Agashe, H. Davoudiasl, G. Perez, and A. Soni, “Warped Gravitons at the LHC and
1210 Beyond,” *Phys. Rev.*, vol. D76, p. 036006, 2007.
- 1211 [32] A. L. Fitzpatrick, J. Kaplan, L. Randall, and L.-T. Wang, “Searching for the Kaluza-Klein
1212 Graviton in Bulk RS Models,” *JHEP*, vol. 09, p. 013, 2007.
- 1213 [33] H. Davoudiasl, J. L. Hewett, and T. G. Rizzo, “Phenomenology of the Randall-Sundrum
1214 Gauge Hierarchy Model,” *Phys. Rev. Lett.*, vol. 84, p. 2080, 2000.
- 1215 [34] T. Gherghetta and A. Pomarol, “Bulk fields and supersymmetry in a slice of AdS,” *Nucl.*
1216 *Phys.*, vol. B586, pp. 141–162, 2000.
- 1217 [35] H. Davoudiasl, J. L. Hewett, and T. G. Rizzo, “Experimental probes of localized gravity:
1218 On and off the wall,” *Phys. Rev.*, vol. D63, p. 075004, 2001.
- 1219 [36] A. Oliveira, “Gravity particles from Warped Extra Dimensions, predictions for LHC,”
1220 2014.
- 1221 [37] CMS Collaboration, “Search for diboson resonances in the $2l2\nu$ final state,” CMS Physics
1222 Analysis Summary CMS-PAS-B2G-16-023, CERN, Geneva, 2017.
- 1223 [38] CMS Collaboration, “Search for heavy resonances decaying to a pair of Higgs bosons in
1224 the four b quark final state in proton-proton collisions at $\sqrt{s} = 13 \text{ TeV}$,” CMS Physics
1225 Analysis Summary CMS-PAS-B2G-16-026, CERN, Geneva, 2017.
- 1226 [39] “Pileup Reweighting Procedure - <https://twiki.cern.ch/twiki/bin/viewauth/CMS/PileupReweighting>,”
- 1228 [40] “Utilities for Accessing Pileup Information for Data - <https://twiki.cern.ch/twiki/bin/view/CMS/PileupJSONFileforData>,”
- 1230 [41] “EGamma POG - Cut based electron ID for Run2 - <https://twiki.cern.ch/twiki/bin/view/CMS/CutBasedElectronIdentificationRun2>,”

- 1232 [42] “EGamma POG - Electron ID recipes for Run2 - <https://twiki.cern.ch/twiki/bin/view/CMS/EgammaIDRecipesRun2>,”
- 1233
- 1234 [43] CMS Collaboration, “Performance of cms muon reconstruction in pp collision events at
1235 $\sqrt{s} = 7\text{TeV}$.” Submitted to *J. Inst.*, 2012.
- 1236 [44] R. Fruhwirth, “Application of kalman filtering to track and vertex fitting,” *Nuclear Instruments and Methods in Physics Research Section A: Accelerators, Spectrometers, Detectors and Associated Equipment*, vol. 262, no. 23, pp. 444 – 450, 1987.
- 1237
- 1238
- 1239 [45] “Reference muon id, isolation and trigger efficiencies for Run-II -
1240 <https://twiki.cern.ch/twiki/bin/view/CMS/MuonReferenceEffsRun2>,”
- 1241 [46] “Tau POG - Tau ID for Run2 - <https://twiki.cern.ch/twiki/bin/viewauth/CMS/-TauIDRecommendation13TeV>,”
- 1242
- 1243 [47] “EGamma POG - Cut based photon ID for Run2 - <https://twiki.cern.ch/twiki/bin/view/CMS/CutBasedPhotonIdentificationRun2>,”
- 1244
- 1245 [48] CMS Collaboration, “Particle-flow event reconstruction in CMS and performance for jets,
1246 taus, and E_T^{miss} ,” no. CMS-PAS-PFT-09-001, 2009.
- 1247 [49] CMS Collaboration, “Commissioning of the particle-flow event reconstruction with the
1248 first LHC collisions recorded in the CMS detector,” no. CMS-PAS-PFT-10-001, 2010.
- 1249 [50] “Pileup Removal Algorithms,” Tech. Rep. CMS-PAS-JME-14-001, CERN, Geneva, 2014.
- 1250 [51] M. Cacciari, G. P. Salam, and G. Soyez, “The anti- k_t jet clustering algorithm,” *JHEP*,
1251 vol. 04, p. 063, 2008.
- 1252 [52] T. C. collaboration, “Determination of jet energy calibration and transverse momentum
1253 resolution in cms,” *Journal of Instrumentation*, vol. 6, no. 11, p. P11002, 2011.
- 1254 [53] “JetMET POG - Jet ID for Run2 - <https://twiki.cern.ch/twiki/bin/view/CMS/JetID>,”
- 1255 [54] “Jetmet pog - jet energy resolution smearing - <https://twiki.cern.ch/twiki/bin/view/cms/jetresolution>,”
- 1256
- 1257 [55] A. J. Larkoski, S. Marzani, G. Soyez, and J. Thaler, “Soft Drop,” *JHEP*, vol. 05, p. 146,
1258 2014.
- 1259 [56] T. K. Arrestad et al., “Identification and calibration of boosted hadronic W/Z bosons at
1260 13 TeV,” tech. rep., AN-2016/215, 2016.
- 1261 [57] S. Chatrchyan et al., “Identification of b-quark jets with the CMS experiment,” *JINST*,
1262 vol. 8, p. P04013, 2013.
- 1263 [58] “BTV POG - B-tagging for Run2 - <https://twiki.cern.ch/twiki/bin/view/CMS/BtagRecommendation80X>,”
- 1264
- 1265 [59] “Methods to apply b-tagging efficiency scale factors,” 2013.